PROCEEDINGS A

rspa.royalsocietypublishing.org

Research

Article submitted to journal

Subject Areas:
mathematical modelling, scattering, acoustics

Keywords:
Debye approximation, modulated dipole, three-dimensional multipole, phase Mach number, Rayleigh scattering

Author for correspondence:
C. J. Chapman
e-mail: c.j.chapman@keele.ac.uk

THE ROYAL SOCIETY
PUBLISHING

Near-field scattering by the method of locally subsonic waves

C. J. Chapman[1], S. C. Hawkins[2]

[1]Department of Mathematics, University of Keele, Staffordshire ST5 5BG, UK
[2]School of Mathematical and Physical Sciences, Macquarie University, Sydney, NSW 2109, Australia

A technique is developed for determining the sound field scattered by a compact body when it is close enough to an acoustic source to be in its near field. Our approach is based on the fact that large regions of many near fields may be well approximated at each point in space by a *subsonic* plane wave (also called an inhomogeneous plane wave, or an evanescent wave). Such a wave is defined by the property that in one direction it propagates with subsonic phase speed, while in a perpendicular direction it has exponential amplitude variation. Hence by defining a canonical problem, compact scattering of a subsonic plane wave, and solving it, we are able to give a unified analytical treatment of many near-field scattering problems. Our approach draws on the formulae of Rayleigh scattering (as applied to an incident field with complex wavenumber) and the asymptotic theory of the wave equation. For an arbitrary three-dimensional multipole, we determine in full detail how its subsonic wave structure depends on the spherical harmonic parameters (m, n), and show that our approach has a very large region of validity.

1. Introduction

Right at the start of the classic work 'Waves in layered media' (1960, 1980), the author Brekhovskikh drew attention to the importance of the inhomogeneous plane wave as a basic component of many acoustic fields, and derived its main properties [1, pp. 3–5]. Principal among these are the basic facts that in one direction, which is the direction of propagation, the phase speed is subsonic, whereas in a perpendicular direction, which is the direction of evanescence, the amplitude decays exponentially with position. Thus a coordinate system

may chosen in which the pressure field is simply

$$p = p_0 \mathrm{e}^{-lx_2} \cos(kx_1 - \omega t), \tag{1.1}$$

where x_1 is the propagation direction and x_2 is the direction of evanescence. It may be assumed that the constants p_0, l, k, and ω are positive, and that in the underlying wave equation satisfied by (1.1), the speed of sound has the constant value c_0. Thus (1.1) represents a wave with propagation speed ω/k in the x_1 direction and a spatial decay rate l in the x_2 direction (or equivalently, a spatial increase at the same rate in the $-x_2$ direction). The quantity p_0 is the amplitude of the wave in the coordinate plane $x_2 = 0$.

Of course, the quantities k and l in this wave are not arbitrary. If we define the free-space wavenumber corresponding to the frequency ω by $k_0 = \omega/c_0$, then substitution of (1.1) into the wave equation gives the basic relation

$$k^2 - l^2 = k_0^2, \tag{1.2}$$

which is simply the dispersion relation corresponding to a sound speed of c_0. It follows that $l = 0$ corresponds to an ordinary plane wave, with sonic phase velocity, whereas $l \neq 0$ gives a propagation speed which is necessarily subsonic (and we may deduce immediately that a supersonic plane wave cannot occur).

From such a humble starting point, the research group led by L. B. Felsen in the 1970s produced a body of work based on the observation that many complicated acoustic fields contain, nevertheless, regions of space in which the field is locally of the simple form (1.1), subject to the proviso that the pair (k, l) satisfying (1.2), which allows one degree of freedom, must be found as part of the solution, and must be allowed to vary (slowly) from one position to another. Thus the subject became susceptible to ray-tracing within the mathematical framework of the WKB method, and the research group solved a number of rather difficult problems by this method. Three papers recording the results are [2–4]—in which the titles reveal a curiosity of the subject in that the name 'inhomogeneous wave' is not always the most appropriate. In many problems, the most important feature of such a wave is its exponential decay in amplitude in a certain direction, in which case the term 'evanescent wave' is used; in other problems it is the propagation (in the perpendicular direction) which is important, and the appropriate term is now 'subsonic wave'. In this latter case, the one degree of freedom referred to above makes possible the definition of a dimensionless parameter which may be called the phase Mach number, and takes values between 0 and 1.

The papers [2–4] and others from the same research group have remained of interest, and are still of value after the interval of 50 years since their publication. Yet they display a particular orientation. Built into the theory in these works is the assumption that the length scales $1/k$ and $1/l$ of the wave (1.1) are small compared with the other scales of variation in the formulation of the problem, so that the background varies slowly in the spatial sense compared with the scale of variation in wave itself, i.e. the wavelength. However, there is a different type of problem in acoustics, in which the length scales occurring in the specification of a problem are much shorter than those in the wave. The prototype of such a problem is Rayleigh scattering, in which an incident plane wave, of the ordinary sonic type, is scattered by an object of dimensions much smaller than the incident wavelength. If this object is an impenetrable hard sphere of radius a, for example, then in the notation above with $k_0 = \omega/c_0$ and $l = 0$, the regime in question is $k_0 a \ll 1$, and a typical result is that the scattered acoustic energy scales with $(k_0 a)^4$ (see, for example, [5, p. 376] or [6, p. 226]). More generally, and especially in aeroacoustics, one refers to scattering (or sound generation) by a compact body, the term indicating that the body is smaller than a free space wavelength, and hence that it is surrounded by an acoustic near field which acts as an intermediate layer between the body itself and the region of space (the acoustic far field) in which the the field may be approximated by a locally plane wave, or by a superposition of a small number of such waves, of the ordinary sonic type.

The idea behind the present paper is that a generalisation of the above Rayleigh scattering problem is available, in which the incident field is a subsonic wave of the type (1.1) rather than an ordinary plane wave, the scatterer being of dimensions small compared with the length-scales $1/k$ and $1/l$ implicit in this wave. Such a problem is relevant to scattering by a small object in many regions of actually occurring acoustic fields, most notably their near fields. Although the generalisation involves no more than taking the incident wavenumber to be complex in existing formulae for Rayleigh scattering [5–9], this does not appear to have been done, and on carrying out the details we obtained an unanticipated result. This is that although in the formulation of the problem there is no rotation in the incident sound field or the scatterer, nevertheless the scattered field rotates, and the rotation can be described in mathematical terms. Particularly, the far field displays both amplitude and phase modulation in the course of its rotation. It is exactly as if part of the scattered field is produced by a rotating (but modulated) point force. We give a complete mathematical description of this phenomenon, including explicit formulae for both the amplitude and phase of the modulation as functions of time. We believe that these results are new.

The structure of the paper is as follows. In §2 the mathematical analysis of the above problem is carried out. In §3 we give precise criteria for what it means for an incident wave field to be well approximated by a locally subsonic wave, and we provide an ansatz, (3.1), for this wave to be locally approximated by the representation (1.1). In §§4–6 we apply this ansatz to three families of incident sound fields, of cylindrical, helical, and three-dimensional multipole type, and in particular, for the multipole field we cover the complete range of spherical harmonic parameter values (m, n), namely $n \geq 0$ and $0 \leq m \leq n$. We have taken care here to provide a full set of numerical plots showing the fidelity of the local approximation, so that the reader has complete information about the numerical accuracy provided by our approach as function of the parameters of the incident field. In this regard, figures 7 and 9 should be regarded as being of very great importance for the work. In §7 we present conclusions and indicate the scope of further work involving our approach, especially in relation to established numerical methods [10,11]. Our approach applies equally to scattering by a small body situated within an edge wave [12] or interfacial wave, but we do not give details of this case here; our focus is on near fields.

A recurring theme throughout the paper is 'phase capture'. In both the first half of the paper, on the canonical scattering problem, and the second half, on the occurrence of subsonic plane waves, our methods and formulae capture the phase with great accuracy, as well as amplitudes. It is this feature which enables us to give such a precise description of the rotation and modulation of the scattered field, and also show, with fully documented accuracy, that the region of a near field which is represented accurately by a field of locally subsonic plane waves can be very extensive indeed.

2. Rayleigh scattering of an incident subsonic wave

We now formulate and solve the canonical problem of the scattering of a subsonic acoustic wave by a small obstacle. The scatterer is assumed to be an impenetrable hard sphere of radius a with its centre at the origin of a cartesian coordinate system (x_1, x_2, x_3). Thus the surface of the sphere is $x_1^2 + x_2^2 + x_3^2 = a^2$, and we denote this surface S. The incident subsonic wave is (1.1), in which the wave parameters are positive and satisfy (1.2), but are otherwise arbitrary. Hence the wave propagates in the positive x_1 direction, evanesces in the positive x_2 direction, and is independent of x_3, so that it has the same form (1.1) in every plane perpendicular to the x_3 axis.

The incident wave may also be written as the real part of $p_0 \exp(-\mathrm{i}\omega t + \mathrm{i}\mathbf{k}\cdot\mathbf{x})$ where $\mathbf{x} = (x_1, x_2, x_3)$ and $\mathbf{k}$ denotes the complex wave vector $(k, \mathrm{i}l, 0)$. This form is convenient because many formulae of wave theory apply for both real and complex wave vectors, and this gives at once ([8, p. 56] or [9, p. 83]) the scattered field in the form

$$p_{\mathrm{s}}(\mathbf{x}, t) \simeq -\frac{p_0}{\rho_0}\frac{m_0}{4\pi r}\frac{\omega^2}{c_0^2}\Big(1 - \frac{3}{2}\frac{\mathbf{k}\cdot\mathbf{x}}{k_0 r}\Big)\mathrm{e}^{-\mathrm{i}\omega(t - r/c_0)}. \tag{2.1}$$

Here $m_0 = 4\pi\rho_0 a^3/3$ is the mass of undisturbed fluid displaced by the sphere, and $r = |\mathbf{x}|$ is the distance from the centre of the sphere to the observation point; the real part of field quantities such as pressure is to be understood. The expression (2.1) requires that it is to be evaluated in the far field, and also that the scatterer is compact. In relation to the parameters (k, l) of the wave (1.1), both of which have the dimensions of the reciprocal of a length, we are therefore led to the requirement, assumed henceforth, that

$$a \ll \min\left(l^{-1},\, k^{-1}\right) \ll |\mathbf{x}|. \tag{2.2}$$

In (2.1) the scattered field is the sum of a monopole and dipole part—in this respect being similar to the field scattered by an ordinary sonic plane wave. However, what is less obvious is the *rotation* of the dipole field, arising from complex $\mathbf{k}$. To bring this out, let us now use the symbol $p_{\rm s}(\mathbf{x}, t)$ for the real part only of (2.1), and write out the scattered field entirely in terms of real quantities as

$$p_{\rm s}(\mathbf{x}, t) \simeq -\frac{p_0}{\rho_0}\frac{m_0}{4\pi r}\frac{\omega^2}{c_0^2}\left\{\cos\omega\tilde{t} - \frac{3}{2}\frac{c_0}{\omega}\left(k\,\hat{\mathbf{x}}\cdot\mathbf{e}_1\cos\omega\tilde{t} + l\,\hat{\mathbf{x}}\cdot\mathbf{e}_2\sin\omega\tilde{t}\right)\right\}. \tag{2.3}$$

Here $(\mathbf{e}_1, \mathbf{e}_2)$ are unit coordinate vectors in the (x_1, x_2) directions, respectively, and $\hat{\mathbf{x}} = \mathbf{x}/r$ is the unit vector in the $\mathbf{x}$ direction. We have also introduced the retarded time $\tilde{t} = t - r/c_0$. The rotation is now evident from the phasing $(\cos\omega\tilde{t}, \sin\omega\tilde{t})$ of the terms in $\hat{\mathbf{x}}\cdot\mathbf{e}_1$ and $\hat{\mathbf{x}}\cdot\mathbf{e}_2$.

(a) General features of the directivity pattern

The scattered field (2.3) has a fully three-dimensional directivity pattern. To see this explicitly, we use a spherical coordinate system (r, θ, ϕ) in which θ is the polar angle measured from the positive x_3 direction (transverse to the incident velocity field), and ϕ is an azimuthal angle in the (x_1, x_2) plane, oriented so that the positive x_1 axis is $\phi = 0$ (the incident direction of propagation) and the positive x_2 axis is $\phi = \pi/2$ (the direction of evanescence). Thus in (2.3) we have

$$\hat{\mathbf{x}}\cdot\mathbf{e}_1 = \sin\theta\cos\phi, \quad \hat{\mathbf{x}}\cdot\mathbf{e}_2 = \sin\theta\sin\phi. \tag{2.4}$$

In what follows, we shall analyse the directivity pattern exhibited by (2.3), and it would possible to write all subsequent formulae in terms of θ and ϕ. However, we shall not do this. The principal results we wish to emphasize are exhibited by the directivity pattern restricted to the (x_1, x_2) plane, i.e. evaluated for $\theta = \pi/2$, and we therefore assume this value of θ henceforth. That is, the crucial angle is ϕ, for which $\phi = 0$ represents the forward scattering direction, and $\phi = \pi$ the direction of back-scatter. It should be remembered, though, how thoroughly non-axisymmetric is the field represented by (2.3); in this respect it differs from the familiar directivity pattern of Rayleigh scattering of an ordinary (sonic) plane wave [9, p. 83]. Quantitatively, the degree of non-axisymmetry is represented by the dependence on θ and the fact the the angle ϕ is not a polar angle about the x_1 axis.

(b) The phase Mach number

To represent the one degree of freedom permitted by the dispersion relation $k^2 - l^2 = (\omega/c_0)^2$, it is convenient to take as a parameter the phase speed ω/k of the wave (1.1), normalised by the phase speed c_0 of an ordinary sonic wave. This gives the phase Mach number M defined by

$$M = \frac{\omega/k}{c_0} = \frac{\omega}{c_0 k}, \tag{2.5}$$

and we immediately obtain a number of basic relations which we shall use repeatedly, most notably

$$\frac{c_0 k}{\omega} = \frac{1}{M}, \qquad \frac{c_0 l}{\omega} = \frac{(1-M^2)^{\frac{1}{2}}}{M}, \qquad \left(\frac{l}{k}\right)^2 = 1 - M^2. \tag{2.6}$$

Since k and l are real, the range of allowed M defined by (2.5) is $0 \leq M \leq 1$, though in formulae with denominator M we envisage the limit $M \to 0$ rather than put $M = 0$ directly.

The phase Mach number is a most useful quantity in what follows. Although defined physically as a dimensionless measure of the propagation speed of the wave (1.1) (in the x_1 direction), it serves also as a parameter to quantify the continuous variation of *any* property between its value for an ordinary sonic wave ($M = 1$) and for a solution of Laplace's equation corresponding to incompressible flow ($M = 0$). The 'very near field' (also called the hydrodynamic near field) is represented by such a solution of Laplace's equation, and as the observation point is moved further out, the local field at such a hypothetically moving point corresponds to increasing values of M, up to a maximum value of $M = 1$, which indicates that the far field has been reached—and then M stays at 1. Thus the value of M is a near-field diagnostic, giving information about the local nature of the field as a function of position. This is explicit in the examples considered in §§4–6.

(c) The directivity function

With the relations (2.6) available, and remembering the decision to restrict ourselves to $\theta = \pi/2$ in (2.4), we find it expedient to define a directivity function $D \equiv D(\phi, \tilde{t})$ by

$$D(\phi, \tilde{t}) = M \cos\omega\tilde{t} - \frac{3}{2}\Big(\cos\phi\cos\omega\tilde{t} + (1 - M^2)^{\frac{1}{2}} \sin\phi \sin\omega\tilde{t}\Big), \tag{2.7}$$

in which M is a parameter. Then the scattered acoustic field (2.3) may be written in the form

$$p_{\mathrm{s}}(\mathbf{x}, t) \simeq -\frac{p_0}{\rho_0}\frac{m_0}{4\pi r}\frac{\omega k}{c_0} D(\phi, \tilde{t}). \tag{2.8}$$

In D, we give the arguments explicitly or omit them according to the emphasis required. There is a degree of choice in the multiplicative factor to be included in the definition of D. The choice in (2.7) is found to be convenient because of its limiting forms: the incompressible limit is simply

$$D(\phi, \tilde{t}) \to -\frac{3}{2}\Big(\cos\phi\cos\omega\tilde{t} + \sin\phi\sin\omega\tilde{t}\Big) = -\frac{3}{2}\cos(\phi - \omega\tilde{t}) \qquad (M \to 0), \tag{2.9}$$

whereas the sonic limit is

$$D(\phi, \tilde{t}) \to \Big(1 - \frac{3}{2}\cos\phi\Big)\cos\omega\tilde{t} \qquad (M \to 1). \tag{2.10}$$

The factor $1 - (3/2)\cos\phi$ in (2.10) agrees with the standard directivity for Rayleigh scattering of a sonic incident wave [9, p. 83].

The directivity D in (2.8) includes complete phase and time-history information about $p_{\mathrm{s}}(\mathbf{x}, t)$; this is needed for analysing the rotational aspect of the scattered field (as is evident already in the term $\cos(\phi - \omega\tilde{t})$ in (2.9)), but it should be borne in mind that other definitions of directivity are in common use, many relating to energy flow rather than a linear expression in the pressure. In the former case, an energy flow directivity would involve the *square* of a quantity related to our D, and would not contain the phase information needed for our purposes.

(d) The rotating modulated dipole

Let us write the directivity function (2.7) in the form

$$D(\phi, \tilde{t}) = D_0(\phi, \tilde{t}) + D_2(\phi, \tilde{t}), \tag{2.11}$$

with monopole contribution

$$D_0(\phi, \tilde{t}) = M\cos\omega\tilde{t} \tag{2.12}$$

and dipole contribution

$$D_2(\phi, \tilde{t}) = A(\tilde{t})\cos(\phi - \alpha(\tilde{t})), \tag{2.13}$$

here written in amplitude-phase form on combining the two non-monopole terms in (2.7). Elementary trigonometry gives the dipole amplitude

$$A(\tilde{t}) = \frac{3}{2}\Big(\cos^2\omega\tilde{t} + (1-M^2)\sin^2\omega\tilde{t}\Big)^{\frac{1}{2}} = \frac{3}{2}\Big(1 - M^2\sin^2\omega\tilde{t}\Big)^{\frac{1}{2}} \tag{2.14}$$

and the relation

$$\tan\alpha = (1-M^2)^{\frac{1}{2}}\tan\omega\tilde{t} \tag{2.15}$$

to be satisfied by the phase function $\alpha(\tilde{t})$. Some care is needed in unwrapping the phase from (2.15), to ensure that the correct multiple of π is included in α to make $\alpha(\tilde{t})$ a continuous function of $\tilde{t}$ over the whole range $-\infty < \tilde{t} < \infty$. Suitable check values are that when

$$\omega\tilde{t} = \Big(0,\ \frac{\pi}{2},\ \pi,\ \frac{3\pi}{2},\ 2\pi\Big) \tag{2.16}$$

we have

$$\alpha(\tilde{t}) = \Big(-\pi,\ -\frac{\pi}{2},\ 0,\ \frac{\pi}{2},\ \pi\Big) \tag{2.17}$$

and

$$D_2(\phi,\tilde{t}) = \frac{3}{2}\Big(-\cos\phi,\ \ -(1-M^2)^{\frac{1}{2}}\sin\phi,\ \ \cos\phi,\ \ (1-M^2)^{\frac{1}{2}}\sin\phi,\ \ -\cos\phi\Big), \tag{2.18}$$

respectively. From the definition (2.13), an arbitrary multiple of 2π may be added to α, and this has been done in figure 1, which also includes the curves $\alpha \pm \pi$, $\alpha \pm 3\pi, \ldots$. Here the continuity of the curves indicates that the phase has been unwrapped correctly.

At any fixed time, the expression (2.13) represents a dipole field, by virtue of the cosine dependence, but this dipole does not have a fixed direction in space, and neither does it have constant amplitude. Let us for the moment exclude the case $M = 1$, which is just the case of an incident sonic plane wave. From figure 1, and also from (2.15), it may be seen that α increases monotonically with time, and therefore the dipole rotates always in the anti-clockwise direction, as viewed in the (x_1, x_2) plane with conventional orientation of axes. However, the rotation rate is far from uniform: and in fact for M close to 1, the last plot in figure 1 shows that the dipole hardly rotates at all for most of the time within its periodic cycle, but then 'whips round' in very short time intervals centred on $\omega\tilde{t} = 0, \pm\pi, \pm 2\pi, \ldots$. This explains how it is possible that when $M = 1$ the field does not rotate, even though the dependence of the field on M is continuous in the whole range $0 \le M \le 1$: the last plot in the figure shows that the limiting behaviour as $M \to 1$ is a set of horizontal and vertical lines, in which the vertical lines have no significance, and horizontal lines in the figure indicate a complete *absence* of rotation.

In summary, the dependence of α on $\tilde{t}$ represents phase modulation, taking a rather extreme form as M increases towards 1, and a relatively tame form as M decreases towards 0. In this latter regime the nearly straight-line form of the α curves (e.g. for $M = 0.1$ in figure 1) indicates rotation at an almost constant angular velocity, approaching a constant angular velocity as $M \to 0$. From the form of (2.13), at each time $\tilde{t}$ the dipole has its main axis in the directions $\alpha(\tilde{t})$ and $\alpha(\tilde{t}) \pm \pi$ in the (x_1, x_2) plane, with direction measured anti-clockwise from the positive x_1 axis, which corresponds to $\alpha = 0$. Since D_2 is a signed quantity and the phase is unwrapped, the direction $\alpha(\tilde{t})$, $\alpha(\tilde{t}) \pm 2\pi, \ldots$ is that of the maximum of the dipole directivity function, and the direction $\alpha(\tilde{t}) \pm \pi$, $\alpha(\tilde{t}) \pm 3\pi, \ldots$ is that of its minimum, as indicated on the first few curves in the figure by the letters a and b.

Turning now to the function $A(\tilde{t})$, we see from its definition (2.13) that this describes *amplitude* modulation of the dipole. Its relatively simple form (2.14) has period π in $\omega\tilde{t}$, revealing an oscillatory variation between the bounds $3/2$ and $3(1-M^2)^{\frac{1}{2}}/2$. For M close to 1, the form of $A(\tilde{t})$ displays a pronounced kink (rapid change of slope) whenever $\sin\omega\tilde{t} = \pm 1$, i.e. for $\omega\tilde{t} = \pi/2, \pi/2 \pm \pi, \pi/2 \pm 2\pi, \ldots$.

Thus the component $D_2(\phi,\tilde{t})$ of the total directivity function $D(\phi,\tilde{t})$ represents a rotating modulated dipole in which the modulation of both amplitude and phase may be described completely in analytical terms. Contour plots of D and D_2 are given in figures 2 and 3. For each,

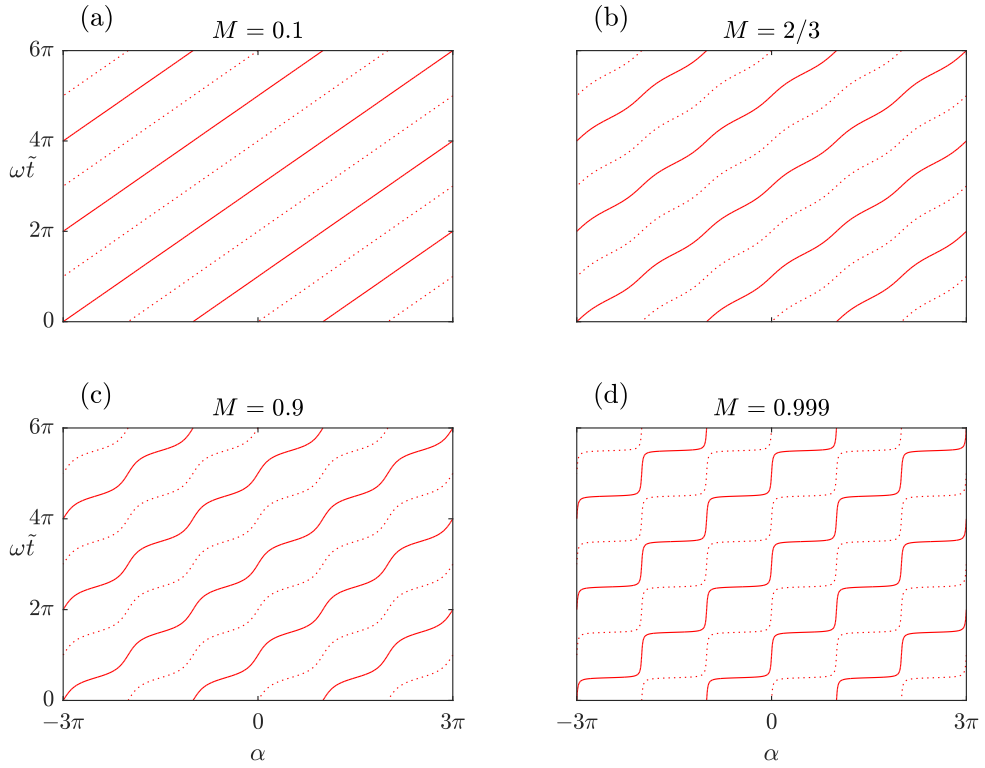

Figure 1. Unwrapping of the phase function α defined by (2.15). Any of the curves $\alpha(\tilde{t})$, $\alpha(\tilde{t}) \pm 2\pi, \ldots$ (solid lines) gives the direction of the maximum of the dipole directivity function D_2 defined by (2.13), whereas any of the curves $\alpha(\tilde{t}) \pm \pi$, $\alpha(\tilde{t}) \pm 3\pi, \ldots$ (dashed lines) gives the direction of the minimum. The origin $(\alpha, \tilde{t}) = (0, 0)$ is always on a dashed curve, consistent with (2.16)–(2.17); this holds for any M.

the α curves of figure 1 may be thought of as providing a kind of skeleton for the fine-textured aspects of the modulation. The monopole term $D_0(\phi, \tilde{t})$ given by (2.12) is simpler still. Given the relevance of the directivity function $D(\phi, \tilde{t})$ (or variants thereof) to a wide variety of near-field and edge wave scattering problems, we feel that the description of the problem we are solving as canonical is justified.

(e) Further details of the directivity

The contour plots in figure 2, while informative about the overall topology of the field, are not best suited for displaying its full quantitative aspects. These are more clearly shown by taking sections of the contour plots at a sequence of fixed times $\tilde{t}$, so that $D(\phi, \tilde{t})$ is presented as a set of functions of ϕ labelled by $\tilde{t}$ as a parameter. This has been done in figure 4, which shows also the envelope of the curves and a number of other significant points, most notably the maxima and minima of the individual curves (as indicated by circles), and of the envelope itself (asterisks). Although the overall impression of the plots is of symmetry about the horizontal axis $D = 0$, this is illusory, because the individual directivity curves do not have this symmetry, being offset by the value $M \cos \omega\tilde{t}$, which is the first term in (2.7).

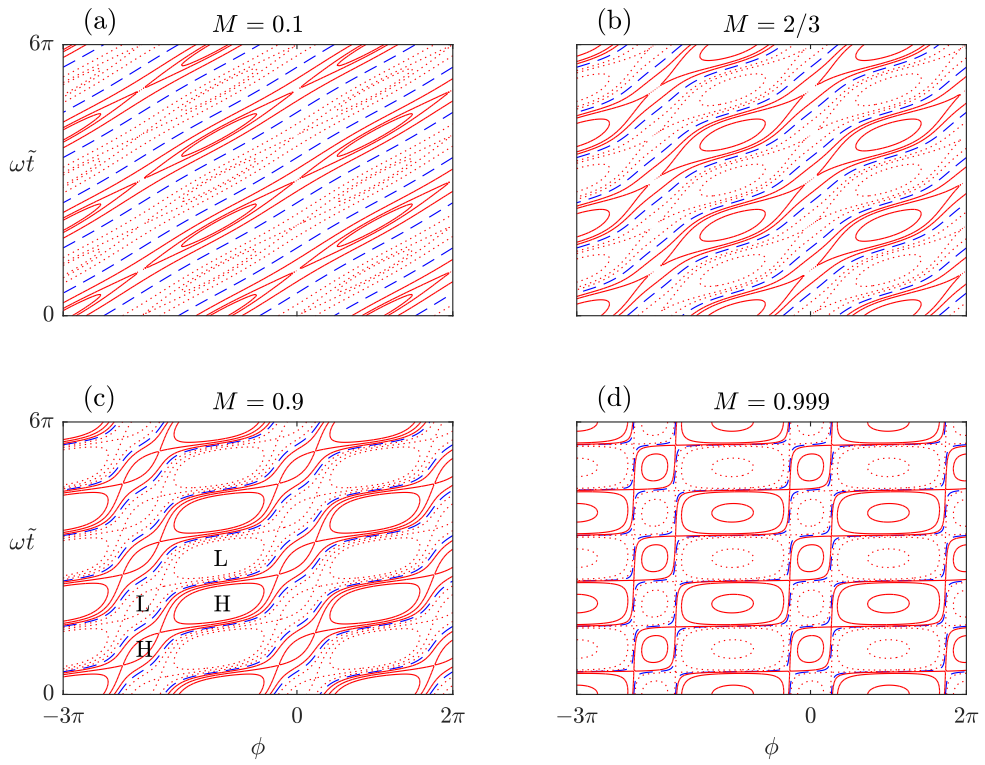

Figure 2. Contour plots of the directivity function $D(\phi, \tilde{t})$ defined by (2.7); (positive, zero, negative) values of D are represented by (solid, dashed, dotted) lines. The pattern of positive and negative D is regular in each plot, as indicated by the symbols H and L representing 'high' and 'low', which are to be imagined repeated throughout. Contour values are (a) $\pm(0, 1, 1.4, 1.5)$; (b) $\pm(0, 0.5, 0.83, 1.5)$; (c) $\pm(0, 0.2, 0.49, 0.83)$; (d) $\pm(0, 0.05, 0.3, 2.0)$. The overall pattern is of diagonal ridges and valleys, undulating in accord with the phase curves shown in figure 1.

(i) The directivity envelope curves

A calculation shows that the envelope of the directivity curves is

$$D = \pm\Big\{\Big(M - \frac{3}{2}\cos\phi\Big)^2 + \Big(\frac{3}{2}\Big)^2(1 - M^2)\sin^2\phi\Big\}^{\frac{1}{2}}. \tag{2.19}$$

Maxima and minima on these envelopes are always to be found where $\phi = 0, \pm\pi$, but for $M \geq 2/3$, there is another family (marked with asterisks), where

$$\cos\phi = \frac{2}{3M}, \qquad D = \pm\frac{\sqrt{5}}{2}(1 - M^2)^{\frac{1}{2}}. \tag{2.20}$$

Equivalently

$$\cos\phi = \pm\frac{2}{3}\Big(1 + \frac{5}{4}\cos^2\omega\tilde{t}\Big)^{\frac{1}{2}} \tag{2.21}$$

and

$$M = \Big(1 + \frac{5}{4}\cos^2\omega\tilde{t}\Big)^{-\frac{1}{2}}, \qquad D = \pm\frac{\sqrt{5}}{2}\Big(1 + \frac{4}{5}\sec^2\omega\tilde{t}\Big)^{-\frac{1}{2}}, \tag{2.22}$$

where $\tilde{t}$ is the parameter value for the directivity curves which touch the maxima and minima of the envelope. Elimination of M from (2.20) gives the closed curve

$$D^2 = \frac{5}{4}\Big\{1 - \Big(\frac{2}{3}\sec\phi\Big)^2\Big\} \tag{2.23}$$

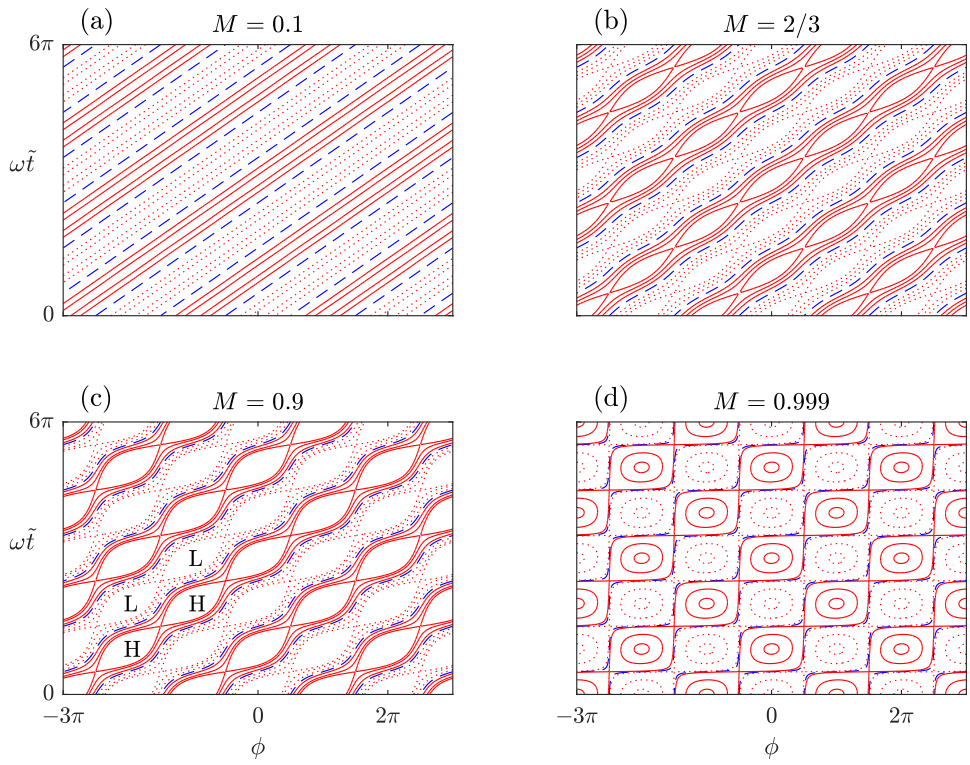

Figure 3. The dipole directivity function $D_2(\phi, \tilde{t})$ defined by (2.13); legend as in figure 2. Contour values are (a) $\pm(0, 1, 1.4, 1.5)$; (b) $\pm(0, 0.5, 0.83, 1.1)$; (c) $\pm(0, 0.2, 0.49, 0.65)$; (d) $\pm(0, 0.07, 0.8, 1.4)$. Ridges and valleys no longer undulate, because the monopole contribution $M \cos\omega\tilde{t}$ is now excluded; cf. the phase curves in figure 1.

in the (ϕ, D) plane, which accordingly is the locus of the asterisks. This curve is shown separately in figure 5; its highest and lowest points correspond to the transition value $M = 2/3$ noted above, and are at $\phi = 0$, $D = \pm 5/6$.

(ii) Directivity maxima and minima

Another short calculation, relating now to the individual directivity curves rather than their envelope, shows that their maxima and minima all lie on the two curves

$$D = \pm\frac{3}{2}\,\frac{(1-M^2)^{\frac{1}{2}}\left\{1-(2M/3)\cos\phi\right\}}{(1-M^2\cos^2\phi)^{\frac{1}{2}}}. \tag{2.24}$$

These curves may be obtained from (2.11)–(2.14) by first writing the maxima and minima in parametric form with $\phi = \alpha(\tilde{t})$ and

$$D = M\cos\omega\tilde{t} \pm A(\tilde{t}) = M\cos\omega\tilde{t} \pm \frac{3}{2}\left(1 - M^2\sin^2\omega\tilde{t}\right)^{\frac{1}{2}}. \tag{2.25}$$

Then elimination of $\tilde{t}$ gives (2.24). The curves are obtained geometrically by joining up the centres of neighbouring circles in figure 4, regarded as present for all $\tilde{t}$ rather than the finite set chosen. For M not too close to 1, the curves are similar to the envelope curves, but closer to the line $D = 0$. As M approaches 1, they develop sharp peaks near $\phi = 0, \pm\pi$, while remaining flat elsewhere; this is evident in figure 4*d*. For $M \geq 2/3$, they have an extra family of maxima and minima, as for the envelope curves, and a geometric argument shows that these are the same points (marked by the

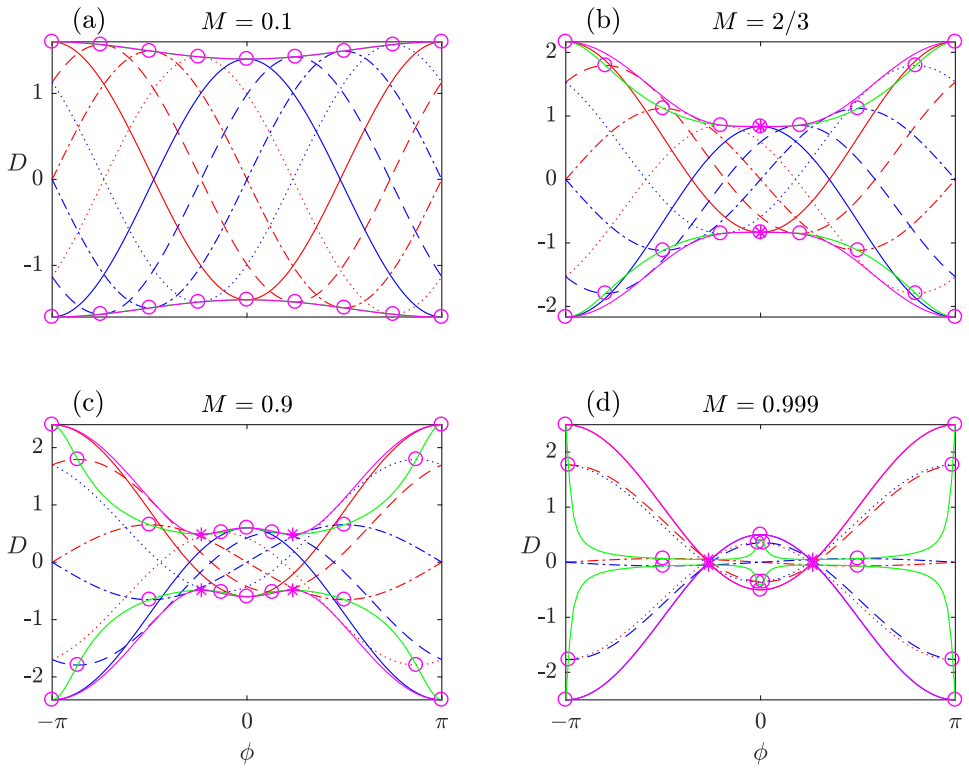

Figure 4. Directivity D as function of ϕ at the sequence of fixed times $\tilde{t}$ given by $\omega\tilde{t} = (0, 1, \ldots, 7)\pi/4$. The maxima and minima of these curves are indicated by circles, which also serve as identifiers: the top row of circles, taken from left to right, lie on the curves for $\omega\tilde{t} = 0, \pi/4, \ldots$, and the final circle is a duplicate of the first, by periodicity. The asterisks, present only for $M \geq 2/3$, have a dual interpretation; they are a second family of maxima and minima, both of the two envelopes of the curves and also of the different pair of curves obtained by joining up the centres of the circles. In each plot, the former consists of the two magenta outer curves, while the latter consists of the two green inner curves; their tangency at the point where the slope is zero is self-evident geometrically, and this feature is also derived analytically in (2.20) and (2.26). Note the different vertical scales; the upper envelopes are plotted on the same scale in figure 5.

asterisks) as for the envelope curves. Analytically, we may confirm this fact from the derivative of (2.24), which is

$$D' = \pm M(1 - M^2)^{\frac{1}{2}} \frac{\{1 - (3M/2)\cos\phi\}\sin\phi}{(1 - M^2\cos^2\phi)^{\frac{3}{2}}}. \tag{2.26}$$

Here the coefficient $2/3$ in the numerator of (2.24) has become $3/2$. Thus $D' = 0$ when $\cos\phi = 2/(3M)$, in agreement $(2.20)_1$ arising from the different function (2.19).

(f) Fixed observation angle

In the contour plots of $D(\phi, \tilde{t})$ shown in figure 2, we may take sections at fixed observation angle ϕ, to obtain functions of $\tilde{t}$ which are dual to the functions of ϕ which we have just calculated. The corresponding plots, with $\omega\tilde{t}$ along the horizontal axis, are shown in figure 6. As the theory is similar to that above, we shall merely summarise the results, in a parallel format.

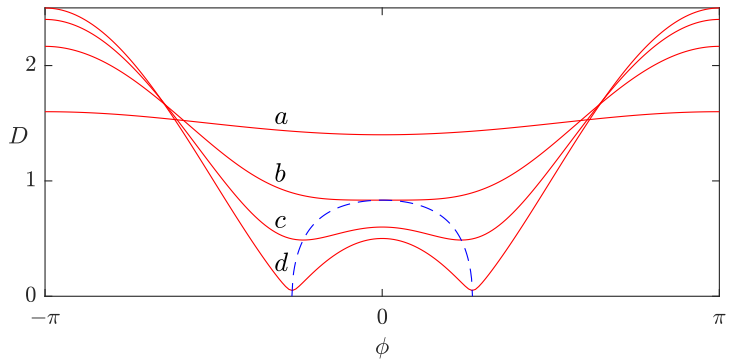

Figure 5. Directivity envelopes and their minima as functions of observation angle ϕ. The solid curves are the upper envelopes in figure 4 as given by (2.19) with the positive sign, and the lettering matches that of figure 4. Thus curves a–d are for $M = 0.1, 2/3, 0.9, 0.999$ respectively. The dashed line is the locus of the minima of the envelopes as M varies; this corresponds to the asterisks in figure 4, defined for $M \geq 2/3$, and given analytically by (2.23). Note that the tangency of curve b and the dashed curve for $M = 2/3$ provides a check of the calculations. The corresponding envelopes as functions of $\omega\tilde{t}$ are similar in form, as evident from the plots given below in figure 6 and the formulae in §2(*f*).

(i) Fixed-angle envelope curves

Vertical asymmetry of the envelope in figure 6 is evident (in contrast to the symmetry of the envelope in figure 4), but nevertheless the individual directivity curves in figure 6 extend as far above the line $D = 0$ as below, as there is no vertical offset. The envelope curves have the equation

$$D = M\cos\omega\tilde{t} \pm \frac{3}{2}\left(1 - M^2\sin^2\omega\tilde{t}\right)^{\frac{1}{2}}, \tag{2.27}$$

and the maxima and minima marked by asterisks have coordinates $(\tilde{t}, D)$ where

$$\cos\omega\tilde{t} = -\frac{2(1-M^2)^{\frac{1}{2}}}{\sqrt{5}M}, \qquad D = \pm\frac{\sqrt{5}}{2}(1-M^2)^{\frac{1}{2}}. \tag{2.28}$$

Equivalently

$$\cos\omega\tilde{t} = \pm\frac{3}{5}\left\{\cos^2\phi - (2/3)^2\right\}^{\frac{1}{2}} \tag{2.29}$$

and

$$M = \pm\frac{2}{3}\sec\phi, \qquad D = \pm\frac{\sqrt{5}}{2}\left\{1 - \left(\frac{2}{3}\sec\phi\right)^2\right\}^{\frac{1}{2}}. \tag{2.30}$$

Recall that the asterisk family exists only for $M \geq 2/3$.

(ii) Fixed angle maxima and minima

Turning now to the individual curves, rather than the envelope, we find that their maxima and minima, marked by circles in figure 6, lie on the curves

$$D = (1-M^2)\,\frac{M\cos\omega\tilde{t} \pm \frac{3}{2}\left(1 + \frac{5M^2}{9(1-M^2)}\sin^2\omega\tilde{t}\right)^{\frac{1}{2}}}{1 - M^2\cos^2\omega\tilde{t}}. \tag{2.31}$$

These curves, like others we have come across, have an extra family of maxima and minima for $M \geq 2/3$, and they are at the same positions as for the envelope curves (2.27). Again, this is geometrically evident, but we have also checked it by differentiation of (2.31). The resulting expression is too long to be given here, but the derivative is in fact zero when $(2.28)_1$ is satisfied. This confirms the identity of these extra stationary points for the curves specified by the different equations (2.27) and (2.31).

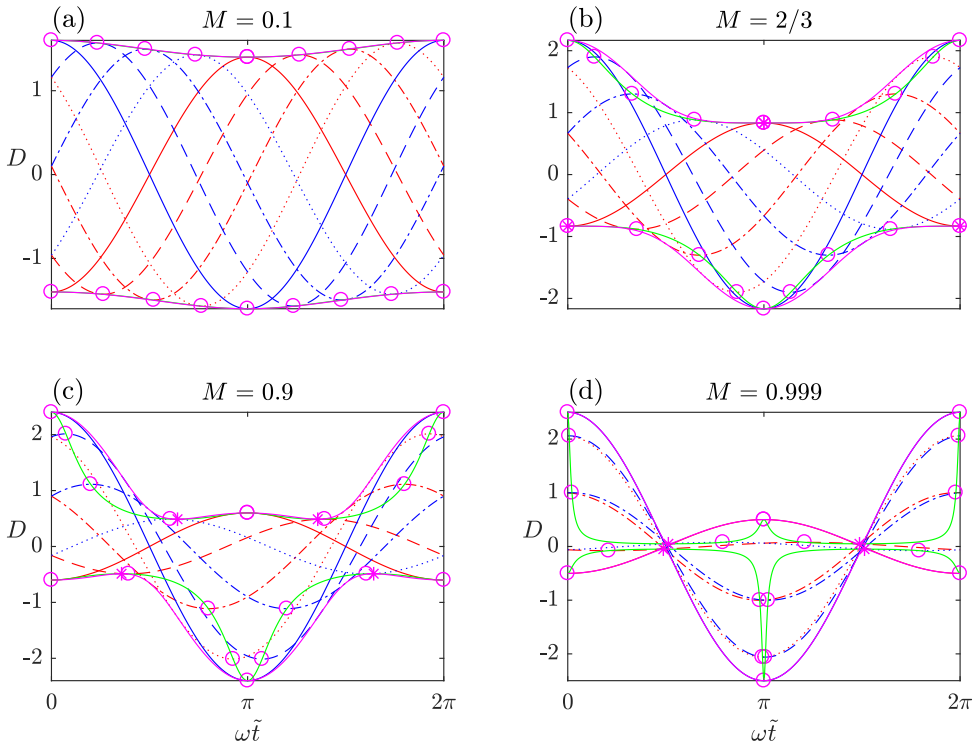

Figure 6. Directivity D as function of $\omega\tilde{t}$ at the sequence of fixed observation angles $\phi = (0, 1, \ldots, 7)\pi/4$ for each value of M; legend as in figure 4, but with interchange of ϕ and $\omega\tilde{t}$, and with formulae relating to the asterisks (for $M \geq 2/3$) now based on (2.28) and (2.31). Full details are in §2(*f*), in parallel format to §2(*e*) for the fixed $\tilde{t}$ curves.

3. Subsonic waves and asymptotic approximations

In order to apply the above results, we need to determine regions of space in which an incident wavefield is well approximated by a locally subsonic wave. This involves finding, for each point in such a region, the corresponding wave parameters (k, l) in the representation (1.1), along with the associated local coordinate system (x_1, x_2, x_3). We have carried this out for three families of incident wavefields, which in increasing order of complexity are of cylindrical, helical, and three-dimensional multipole type. These incident fields are defined globally, in the appropriate separable coordinate system, and so have known analytical forms. In particular, a three-dimensional multipole involves an associated Legendre polynomial, labelled by two integer parameters (m, n), and we analyse such multipole fields for the complete range of parameter values, namely $n \geq 0$ and $0 \leq m \leq n$.

In what follows, our emphasis is on detailed mathematical derivations. Readers whose main interest is in the results will find the most important of these by looking ahead to (4.6)–(4.7) for cylindrical waves; (5.3)–(5.4) for helical waves; and, in the case of three-dimensional multipoles, (6.11)–(6.13) along with (6.15)–(6.16) for (equatorial, near) waves; (6.21)–(6.22) for (polar, near) waves; (6.24)-(6.25) for (polar, far) waves; and (6.27)–(6.28) for (equatorial, far) waves. For all of these, the local coordinate system is determined explicitly by (3.5), and the phase Mach number is presented as a function of position.

The term 'well approximated' will be used in a precise sense involving two criteria which we insist must both be satisfied simultaneously. The first is that the mathematical expression for the locally subsonic wave must arise from an asymptotic approximation in which the leading term gives a wave of the form (1.1) for which the dispersion relation (1.2) is satisfied *exactly*.

This criterion is mathematical, but the second is practical: on a conventional plot we regard the exact waveform as well approximated only at points where the exact and approximate curves are *indistinguishable or nearly so*. Despite the strictness of this latter criterion, especially in relation to the phase, we find that the size of the well-approximated region is much larger than might be expected—a consequence of the particular asymptotic approximations that we use. These are of a type which may be called 'phase capturing', in that they represent the phase to extremely high accuracy over a very extended region.

Although the examples are for rotating fields, we should point out that a non-rotating field may be regarded as a circumferential standing wave, i.e. a superposition of two sound fields rotating in opposite directions. That is, a factor such as $\mathrm{e}^{-\mathrm{i}\omega t}\cos m\phi$ may be written as half the sum of $\mathrm{e}^{-\mathrm{i}(\omega t\pm m\phi)}$, corresponding to clockwise and anti-clockwise rotation, and the total scattered field is then obtained by summation at the end.

(a) Regions of locally plane waves

The method we adopt to find regions of locally plane waves is to use asymptotic approximations to the incident pressure field of the form

$$\tilde{p}(\tilde{\mathbf{x}},t)\simeq P_0\,\mathrm{e}^{-\mathrm{i}\omega t}\,\mathrm{e}^{\Phi_{\mathrm{L}}(\tilde{\mathbf{x}})+\mathrm{i}\Phi_{\mathrm{K}}(\tilde{\mathbf{x}})}, \tag{3.1}$$

where $(\Phi_{\mathrm{L}}(\tilde{\mathbf{x}}),\,\Phi_{\mathrm{K}}(\tilde{\mathbf{x}}))$ are rapidly varying functions. This has the precise meaning that $(\Phi_{\mathrm{L}},\Phi_{\mathrm{K}})$ also depend on parameters which are formally taken to be large. These parameters are specified explicitly in each case. The quantity P_0 is a slowly varying function of $\tilde{\mathbf{x}}$ and is in general complex.

The functions $(\Phi_{\mathrm{L}},\Phi_{\mathrm{K}})$ must satisfy two conditions. The first is a condition on their gradients, $(\nabla\Phi_{\mathrm{L}},\nabla\Phi_{\mathrm{K}})$, which must satisfy

$$\left|\nabla\Phi_{\mathrm{K}}\right|^2-\left|\nabla\Phi_{\mathrm{L}}\right|^2=\left(\frac{\omega}{c_0}\right)^2=k_0^2,\qquad \nabla\Phi_{\mathrm{K}}\cdot\nabla\Phi_{\mathrm{L}}=0. \tag{3.2}$$

This condition implies that the local behaviour of (3.1) is that of a plane wave of the form (1.1) where

$$l=\left|\nabla\Phi_{\mathrm{L}}\right|,\qquad k=\left|\nabla\Phi_{\mathrm{K}}\right|, \tag{3.3}$$

and the local coordinates (x_1,x_2) in (1.1) correspond to axis directions $(\nabla\Phi_{\mathrm{K}},-\nabla\Phi_{\mathrm{L}})$. The third coordinate x_3 is such that (x_1,x_2,x_3) form a right-handed coordinate system, and so the x_3 direction is that of the vector product $\nabla\Phi_{\mathrm{K}}\times(-\nabla\Phi_{\mathrm{L}})$. This first condition is the mathematical expression of the first criterion just given. The second condition concerns the *values* of $(\Phi_{\mathrm{L}},\Phi_{\mathrm{K}})$, and also of P_0, rather than their gradients, and is that when (3.2) is used to approximate the exact incident field, it satisfies the second criterion we gave, that the exact and approximate waveforms are indistinguishable or nearly so on a conventional plot.

The relations (3.3) for (l,k) follow from a local Taylor expansion of the rapidly varying terms in (3.1). If we evaluate these terms at $\tilde{\mathbf{x}}+\delta\tilde{\mathbf{x}}$ rather than $\tilde{\mathbf{x}}$, the terms linear in $\delta\tilde{\mathbf{x}}$ are

$$\delta\tilde{\mathbf{x}}\cdot\nabla\Phi_{\mathrm{L}}+\mathrm{i}\,\delta\tilde{\mathbf{x}}\cdot\nabla\Phi_{\mathrm{K}} \tag{3.4}$$

and we may put

$$\nabla\Phi_{\mathrm{L}}=-l\,\mathbf{e}_2,\quad \nabla\Phi_{\mathrm{K}}=k\,\mathbf{e}_1 \tag{3.5}$$

where $(\mathbf{e}_1,\mathbf{e}_2)$ are the first two unit coordinate vectors in a local coordinate system (x_1,x_2,x_3) with origin at $\tilde{\mathbf{x}}$. Let us also put $P_0=|P_0|\mathrm{e}^{\mathrm{i}\alpha}$, so that α is the phase of P_0; both $|P_0|$ and α depend slowly on $\tilde{\mathbf{x}}$ Then the incident pressure field, evaluated at $\tilde{\mathbf{x}}+\delta\tilde{\mathbf{x}}$ and with local linearisation of the rapidly varying terms, takes the form

$$\tilde{p}\simeq|P_0|\,\mathrm{e}^{\mathrm{i}\alpha}\mathrm{e}^{-\mathrm{i}\omega t}\,\mathrm{e}^{\Phi_{\mathrm{L}}(\tilde{\mathbf{x}})+\mathrm{i}\Phi_{\mathrm{K}}(\tilde{\mathbf{x}})}\mathrm{e}^{-lx_2+\mathrm{i}kx_1} \tag{3.6}$$

in the local coordinate system. Here $\tilde{\mathbf{x}}$ is regarded as fixed, and the terms in (x_1,x_2) give the dependence of the pressure on position in the neighbourhood of $\tilde{\mathbf{x}}$. If we change the time origin

by defining $t' = t - (\alpha + \Phi_{\rm K})/\omega$, and take the real part of (3.6), the result is

$$\mathrm{Re}(\tilde{p}) \simeq |P_0|\, \mathrm{e}^{\Phi_{\rm L}} \mathrm{e}^{-lx_2} \cos(kx_1 - \omega t'). \tag{3.7}$$

This is of the form (1.1) with $p_0 = |P_0|\, \mathrm{e}^{\Phi_{\rm L}}$ and with t' for t, so that we have justified the expressions for l and k given in (3.3), and their relation to local axes defined by (3.5). The phase Mach number M is given in terms of l or k by any of the relations (2.6).

4. A cylindrical sound field

Turning now to our first example, we consider a rotating sound field of a type which is basic in the theory of aircraft noise, for example [13]. This is the pressure field given in cylindrical coordinates $(\tilde{r}, \tilde{\phi}, \tilde{z})$ by

$$\tilde{p} = \tilde{p}_0\, \mathrm{e}^{-\mathrm{i}(\omega t - m\tilde{\phi})}\, J_m\left(\frac{\omega \tilde{r}}{c_0}\right), \tag{4.1}$$

where m is a positive integer, formally regarded as large. The field is defined throughout three-dimensional space, but does not depend on $\tilde{z}$. Although (4.1) contains the Bessel function J_m, we could equally take Y_m or $H_m^{(1)}$, for example, with only minor changes in what follows. The last of these is defined by $H_m^{(1)} = J_m + \mathrm{i}Y_m$. The choice J_m is appropriate to many studies of aeroengine noise, and $H_m^{(1)}$ is needed for a field satisfying a far-field radiation condition with time dependence $\mathrm{e}^{-\mathrm{i}\omega t}$. We imagine that a small scatterer is placed in the incident field (4.1).

The combination $\omega t - m\tilde{\phi}$ in (4.1) shows that the field is rotating; if this term is thought of as representing a solid-body rotation at angular rotation rate ω/m, we may define a sonic radius

$$\tilde{r}_0 = \frac{mc_0}{\omega} = \frac{m}{k_0} \tag{4.2}$$

at which the azimuthal motion is at the speed of sound c_0. Thus the Bessel function in (4.1) may be written in the alternative form $J_m(m\tilde{r}/\tilde{r}_0)$, showing that the transition from 'argument less than order' to 'argument greater than order' occurs at $\tilde{r} = \tilde{r}_0$, i.e. at the sonic radius. For cylindrical fields, we use the sonic radius as the boundary between the near and far field, so that the near field is defined region within the 'sonic cylinder' $\tilde{r} < \tilde{r}_0$ centred on the $\tilde{z}$ axis, and the far field is the region outside this cylinder.

(a) Near-field asymptotics of cylindrical field

The asymptotic approximation we use for the Bessel function $J_m(x)$ when $m > 0$ and $0 < x < m$ is

$$J_m(x) \simeq \frac{1}{(2\pi)^{\frac{1}{2}}} \frac{\mathrm{e}^{\chi_{\rm n}(x)}}{(x_0^2 - x^2)^{\frac{1}{4}}} \qquad (m > 0), \tag{4.3}$$

where

$$x_0 = m, \qquad \chi_{\rm n}(x) = (x_0^2 - x^2)^{\frac{1}{2}} - x_0 \ln\left(\frac{x_0 + (x_0^2 - x^2)^{\frac{1}{2}}}{x}\right), \tag{4.4}$$

and the derivative of $\chi_{\rm n}$, needed for the gradients in (3.2), is

$$\frac{\mathrm{d}\chi_{\rm n}}{\mathrm{d}x} = \frac{(x_0^2 - x^2)^{\frac{1}{2}}}{x}. \tag{4.5}$$

Note that $\chi_{\rm n}$ is negative, but its derivative is positive. The subscript n refers to the near field. This is the Debye approximation given in [14, §10.19(ii)], written in different variables. Throughout the paper we use x as a generic argument for defining a function, and indicate the boundary between different types of approximation by the subscript 0. Here, the domain of (4.3) is $0 < x < x_0$ with $x_0 = m$. Such a point as x_0 is a turning point in the underlying differential equation for $J_m(x)$, namely Bessel's equation of order m [15].

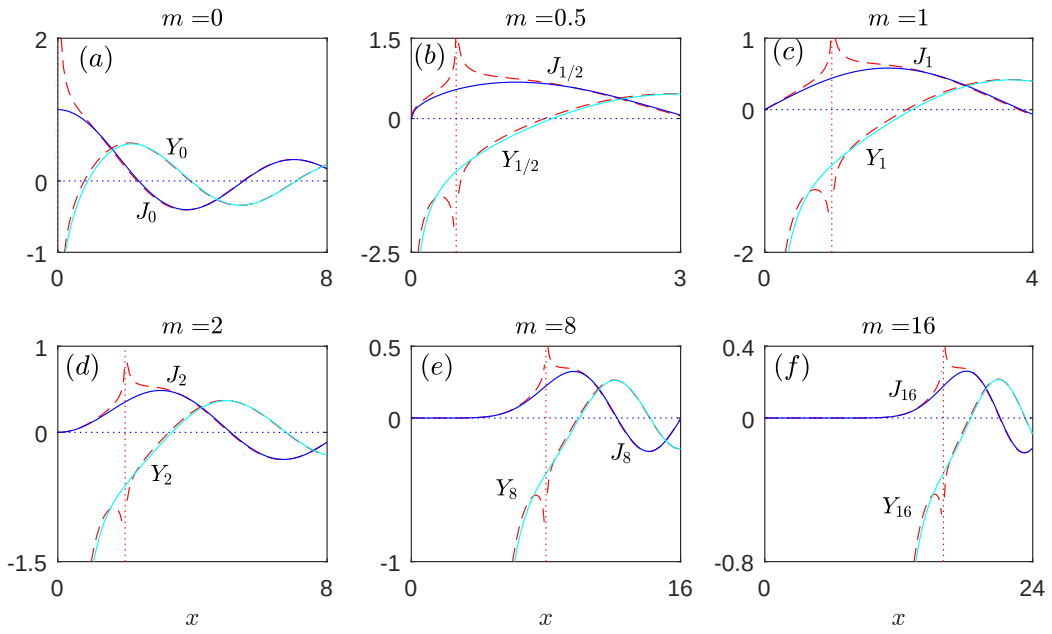

Figure 7. Bessel functions $J_m(x)$ and $Y_m(x)$ for a range of values of m; solid lines are the exact curves, and dashed lines are the asymptotic approximations defined in §4(a, b). The vertical dotted line is at the turning point $x = x_0 = m$. Note the similarity of the plots, and the high accuracy of the approximations except near the turning point, even for small m.

With the aid of (4.3) evaluated at $x = \omega\tilde{r}/c_0 = m\tilde{r}/\tilde{r}_0$, we find that the asymptotic approximation to the near field of (4.1) is of the form (3.1) with

$$P_0 = \frac{\tilde{p}_0}{(2\pi m)^{\frac{1}{2}}} \frac{1}{\{1-(\tilde{r}/\tilde{r}_0)^2\}^{\frac{1}{4}}}, \qquad \Phi_{\mathrm{L}} = \chi_{\mathrm{n}}(m\tilde{r}/\tilde{r}_0), \qquad \Phi_K = m\tilde{\phi}. \tag{4.6}$$

The gradient relations (3.2) now follow at once, so that we have verified the first of the conditions in §3(a) for the near field of (4.1) to be a region of locally subsonic plane waves. In particular, the wave parameters are

$$l = \frac{\partial \Phi_{\mathrm{L}}}{\partial \tilde{r}} = \frac{m\{1-(\tilde{r}/\tilde{r}_0)^2\}^{\frac{1}{2}}}{\tilde{r}}, \qquad k = \frac{1}{\tilde{r}}\frac{\partial \Phi_{\mathrm{K}}}{\partial \tilde{\phi}} = \frac{m}{\tilde{r}}. \tag{4.7}$$

Since m is formally large, these expressions confirm that the exponential term in (3.1) is rapidly varying. In the local coordinate system, $\mathbf{e}_1$ is in the direction of increasing $\tilde{\phi}$, and $\mathbf{e}_2$ is in the direction of decreasing $\tilde{r}$; this corresponds to the fact that the field (4.1) is rotating in the anti-clockwise direction (as conventionally represented in polar coordinates), and the value of the Bessel function decreases towards the origin. From (2.6), the phase Mach number is $M = \tilde{r}/\tilde{r}_0$. This is simply the radial position scaled with the sonic radius, a fact which is geometrically evident from the rotation of the field.

(b) Numerical accuracy of Bessel function approximations

We have just seen that use of approximation (4.3) to the Bessel function in (4.1) gives a field of locally subsonic plane waves in the sonic cylinder $\tilde{r} < \tilde{r}_0$ according to the first criterion in §3. But what about the second criterion, that the exact and approximate waveforms should be indistinguishable or nearly so on a conventional plot? To answer this question requires us to

produce a series of plots of $J_m(x)$ for a number of values of m, and superpose on each the approximation (4.3) to determine, for each m, the range of x for which it is accurate.

As we shall later need the corresponding approximations for $x > m$ and also for Y_m and $H_m^{(1)}$, we present them now, and discuss their level of accuracy together, since this has a consistent pattern as revealed in figure 7. The approximation for $J_m(x)$ when $m \geq 0$ and $x > m$ is

$$J_m(x) \simeq \left(\frac{2}{\pi}\right)^{\frac{1}{2}} \frac{\cos\{\psi_{\rm f}(x) - \pi/4\}}{(x^2 - x_0^2)^{\frac{1}{4}}} \qquad (m \geq 0), \tag{4.8}$$

where

$$x_0 = m, \qquad \psi_{\rm f}(x) = (x^2 - x_0^2)^{\frac{1}{2}} - x_0 \cos^{-1}\left(\frac{x_0}{x}\right), \tag{4.9}$$

and the subscript f refers to the far field. The derivative of $\psi_{\rm f}$ needed for gradients is

$$\frac{{\rm d}\psi_{\rm f}}{{\rm d}x} = \frac{(x^2 - x_0^2)^{\frac{1}{2}}}{x}. \tag{4.10}$$

Both $\psi_{\rm f}$ and its derivative are positive. The corresponding far-field approximations to $Y_m(x)$ and $H_m^{(1)}(x)$ in the region $x > m \geq 0$, are of the same form as (4.8) but with $\sin(\psi_{\rm f} - \pi/4)$ and $\exp\{{\rm i}(\psi_{\rm f} - \pi/4)\}$ instead of $\cos(\psi_{\rm f} - \pi/4)$. The near-field approximation to $Y_m(x)$ for $m > 0$ and $0 < m < x$ is

$$Y_m(x) \simeq -\left(\frac{2}{\pi}\right)^{\frac{1}{2}} \frac{{\rm e}^{-\chi_{\rm n}(x)}}{(x_0^2 - x^2)^{\frac{1}{4}}} \qquad (m > 0), \tag{4.11}$$

with $x_0 = m$ and $\chi_{\rm n}(x)$ as defined in (4.4). Recall that $\chi_{\rm n}$ is negative, but its derivative is positive. All these approximations are of the Debye type as given in [14, §10.19(ii)], after a change of variable. Symbols in ψ represent angles, whereas symbols in χ represent terms appearing in the logarithm of an amplitude. The near-field approximation to $H_m^{(1)} = J_m + {\rm i}Y_m$ is obtained by combining (4.3) and (4.11) for the near fields of J_m and Y_m separately. Since m is formally large and $\chi_{\rm n}$ is negative, it follows that J_m is exponentially smaller than Y_m here, and so in the near field we may take $H_m^{(1)} \simeq {\rm i}Y_m$ with Y_m approximated by (4.11).

Figure 7 plots J_m and Y_m for $m = 0, 1/2, 1, 2, 8, 16$ and superposes the approximations as dashed lines. The turning point $x = m$ is marked by the vertical dotted red line; this is not marked for $m = 0$ because there is then no turning point, so that (4.3) and (4.11) no longer apply (i.e. there is no near field for $m = 0$). Both J_m and Y_m are well approximated by the asymptotic formulae everywhere except within about a quarter wave of the turning point—a remark which holds good independently of m, and in particular is true for $m = 0$. At first sight, this appears to contradict the usual statement that the Debye formulae are large-m approximations. In reality, there is no contradiction. The asymptotic theory shows that a large value of m is a sufficient condition for the validity of the approximations, but this alone does not address the question of whether such a condition is necessary. The plots show that this depends on the value of x, a matter made explicit in our display of functions of x at fixed m, rather than functions of m at fixed x.

That part of J_m to the left of the turning point in the plots corresponds to the subsonic waves forming the near field of (4.1). The part to the right corresponds to ordinary sonic waves in the far field. In the theory we are presenting, the boundary between the near field and the far field is quite sharp (two one-quarter waves), but of course not completely so. We do not give further details, as the subject is covered by the theory of the Airy function which provides a uniform approximation about the turning point in a local $m^{1/3}$ scaling [15]. A point to emphasise is that for our purposes we prefer non-uniform approximations, of the Debye type, because these give subsonic and sonic plane waves explicitly. We do not wish to 'improve' the approximations to make them uniform, because this would introduce corrections which are not of plane wave type, and so hide the plane wave structure we are interested in.

Returning now to (4.6), the relevant plots in figure 7 are (c)–(f), for $m = 1, 2, 8, 16$. The turning point $x = m$ at the vertical dashed line is equivalent to the boundary $\tilde{r} = \tilde{r}_0$ of the sonic cylinder, and approximation (4.3) is the dashed red curve in the upper left in each case. It can be seen in the

figure that the near field of $J_m(x)$ is well approximated by (4.3) except when x approaches the turning point, equivalent to $\tilde{r}$ approaching the sonic cylinder. Thus subsonic waves are present everywhere within the sonic cylinder apart from within a quarter wave of the sonic radius, and the results of §2 are applicable for scatterers in this region. The plots give full quantitative details, because $x = m\tilde{r}/\tilde{r}_0$.

5. A helical sound field

In fully three-dimensional problems, a rotating sound field is often of helical type, rather than being essentially planar, and then (4.1) is replaced by

$$\tilde{p} = \tilde{p}_0 \, \mathrm{e}^{-\mathrm{i}(\omega t - m\tilde{\phi} - k_z \tilde{z})} \, J_m\left(\frac{m\tilde{r}}{\tilde{r}_1}\right), \tag{5.1}$$

where k_z and $\tilde{r}_1$ are taken to be positive and related via the dispersion relation

$$k_z^2 + \left(\frac{m}{\tilde{r}_1}\right)^2 = \left(\frac{\omega}{c_0}\right)^2 = k_0^2, \tag{5.2}$$

but are otherwise arbitrary. The boundary between the near and far field is at $\tilde{r} = \tilde{r}_1$, which may be thought of as defined by (5.2), and the asymptotic approximation to the near field is of the form (3.1) with

$$P_0 = \frac{\tilde{p}_0}{(2\pi m)^{\frac{1}{2}}} \frac{1}{\{1 - (\tilde{r}/\tilde{r}_1)^2\}^{\frac{1}{4}}}, \qquad \Phi_{\mathrm{L}} = \chi_{\mathrm{n}}(m\tilde{r}/\tilde{r}_1), \qquad \Phi_K = k_z\tilde{z} + m\tilde{\phi}. \tag{5.3}$$

With the aid of the dispersion relation (5.2), the gradient relations (3.2) now follow, so that the near field of (5.1) is a region of locally subsonic plane waves. The wave parameters are

$$l = \frac{\partial \Phi_{\mathrm{L}}}{\partial \tilde{r}} = \frac{m\{1 - (\tilde{r}/\tilde{r}_1)^2\}^{\frac{1}{2}}}{\tilde{r}}, \qquad k = |\nabla \Phi_{\mathrm{K}}| = \left\{\left(\frac{m}{\tilde{r}}\right)^2 + k_z^2\right\}^{\frac{1}{2}}. \tag{5.4}$$

In the local coordinate system, (3.5) shows that $\mathbf{e}_1$ has components $(m/(kr), k_z/k)$ in the directions of increasing $(\tilde{\phi}, \tilde{z})$, corresponding to the anti-clockwise helical motion represented by (5.1), and $\mathbf{e}_2$ is in the direction of decreasing $\tilde{r}$, corresponding to the decrease in amplitude of the Bessel function towards the $\tilde{z}$ axis. From (2.6) and the dispersion relation (5.2), the phase Mach number M satisfies

$$\frac{1}{M^2} = 1 + \frac{m^2\{1 - (\tilde{r}/\tilde{r}_1)^2\}}{(\omega\tilde{r}/c_0)^2}, \tag{5.5}$$

from which it follows that $M < 1$ in the near-field cylinder $\tilde{r} < \tilde{r}_1$, as expected. The accuracy of the near-field approximation based on (5.3) is as for the cylindrical sound field in §4, but with $\tilde{r}_1$ instead of $\tilde{r}_0$, and with $x = m\tilde{r}/\tilde{r}_1$ in the plots shown in figure 7. It may be checked that all the formulae of this section reduce to those in §4(a) when $k_z = 0$, because $\tilde{r}_1 = \tilde{r}_0$ in this case, from the dispersion relation (5.2). In particular, (5.5) then simplifies to $M = \tilde{r}/\tilde{r}_0$, as before.

6. Fields of three-dimensional multipole type

A typical multipole wave field in three dimensions may be written

$$\tilde{p} = \tilde{p}_0 \, \mathrm{e}^{-\mathrm{i}(\omega t - m\tilde{\phi})} \, P_n^m(\cos\tilde{\theta}) \, h_n^{(1)}\left(\frac{\omega\tilde{R}}{c_0}\right) \tag{6.1}$$

in a spherical coordinate system $(\tilde{R}, \tilde{\theta}, \tilde{\phi})$ with polar angle $\tilde{\theta}$ and azimuthal angle $\tilde{\phi}$. Here P_n^m is the associated Legendre polynomial of degree n and order m, these taken to be positive integers

or zero with $m \leq n$, and $h_n^{(1)}$ is the spherical Hankel function defined by

$$h_n^{(1)}(x) = \left(\frac{\pi}{2x}\right)^{\frac{1}{2}} H^{(1)}_{n+1/2}(x). \tag{6.2}$$

We sometimes omit the qualifier 'associated', and regard the term Legendre polynomial as referring implicitly to an associated Legendre polynomial. The definition of P_n^m is taken to be that in [14], which differs by a factor of $(-1)^m$ from that in [7].

Many variants of (6.1) arise in applications, involving the other family of Legendre polynomials Q_n^m or the other spherical Hankel and Bessel functions $h_n^{(2)}$, j_n, and y_n, depending on the radiation and boundary conditions appropriate to the problem at hand. Our remarks apply to all such three-dimensional multipoles, but for definiteness we shall concentrate on (6.1). As a notational convenience, we regard the polar coordinates as corresponding to a cartesian system $(\tilde{x}, \tilde{y}, \tilde{z})$ in the usual way, so that the polar axis $\tilde{\theta} = 0$ is the positive $\tilde{z}$ axis, the horizontal plane $\tilde{\theta} = \pi/2$ is the $(\tilde{x}, \tilde{y})$ plane (i.e. $\tilde{z} = 0$), and the half-plane $\tilde{\phi} = 0$ is the meridional half plane $(\tilde{x}, \tilde{z})$ with $\tilde{x} \geq 0$. In addition, we have available the cylindrical coordinates $(\tilde{r}, \tilde{\phi}, \tilde{z})$, where $\tilde{r} = (\tilde{x}^2 + \tilde{y}^2)^{\frac{1}{2}} = \tilde{R}\sin\tilde{\theta}$.

(a) Preliminary example of a multipole field

To fix ideas, let us take $n = 16$, $m = 8$, and plot the real part of (6.1) in the three coordinate surfaces corresponding to the cylindrical system, namely the meridional half-plane $\tilde{\phi} = 0$, the horizontal plane $\tilde{z} = 0$, and cylindrical surfaces of fixed $\tilde{r}$. This is done in figure 8, in length units of the sonic radius $\tilde{r}_0 = mc_0/\omega = m/k_0$ as defined in (4.2), in the form of contour plots of the real part of $\tilde{p}$. In regard to the meridional plot, figure 8*a*, we should point out that whichever meridional half-plane is chosen (i.e., whichever value of $\tilde{\phi}$), the corresponding plot always has the same general form as that shown, but with different phase. Taking the sections in figure 8 as a whole, it can be seen that the alternating regions of high and low pressure in the near field are arranged rather like the segments of an orange, with a transition zone forming its peel. The meridional boundaries of the near-field segments are almost planar, as indicated by the set of straight spoke-like contours in figure 8*b*, and by the straight vertical contours in figure 8*c*; this is perhaps surprising in a rotating wave field. Related figures for $m = n$ are in [16,17].

(b) Asymptotics of associated Legendre polynomials

Our aim now is to find regions of space in which the multipole (6.1) may be approximated by a subsonic wave of the form (3.1) in which $\Phi_{\mathrm{L}}(\tilde{\mathbf{x}})$ and $\Phi_{\mathrm{K}}(\tilde{\mathbf{x}})$ satisfy the gradient relations (3.2). This requires the use of asymptotic approximations to the associated Legendre polynomials, and we now present these in a way which emphasizes their similarity of structure to those given earlier for the Bessel functions.

Corresponding to the trigonometric form (4.8), we have the asymptotic approximation, for n and m formally large,

$$P_n^m(x) \simeq \left(\frac{2}{\pi}\right)^{\frac{1}{2}} a_{nm} \frac{\cos\{\psi_{\mathrm{e}}(x) + \pi/4\}}{(\hat{x}_0^2 - x^2)^{\frac{1}{4}}} \qquad (m > 0; \quad 0 \leq x < \hat{x}_0) \tag{6.3}$$

where

$$\hat{x}_0 = \frac{(N^2 - m^2)^{\frac{1}{2}}}{N}, \qquad \psi_{\mathrm{e}}(x) = -N\cos^{-1}\left(\frac{x}{\hat{x}_0}\right) + m\cos^{-1}\left(\frac{x/(1-x^2)^{\frac{1}{2}}}{\hat{x}_0/(1-\hat{x}_0^2)^{\frac{1}{2}}}\right), \tag{6.4}$$

and $N = n + \frac{1}{2}$. The subscript e on the angular variable ψ_{e} stands for 'equatorial', a notation which reflects the fact that (6.3) is suitable for a region surrounding the equatorial plane $\tilde{\theta} = \pi/2$

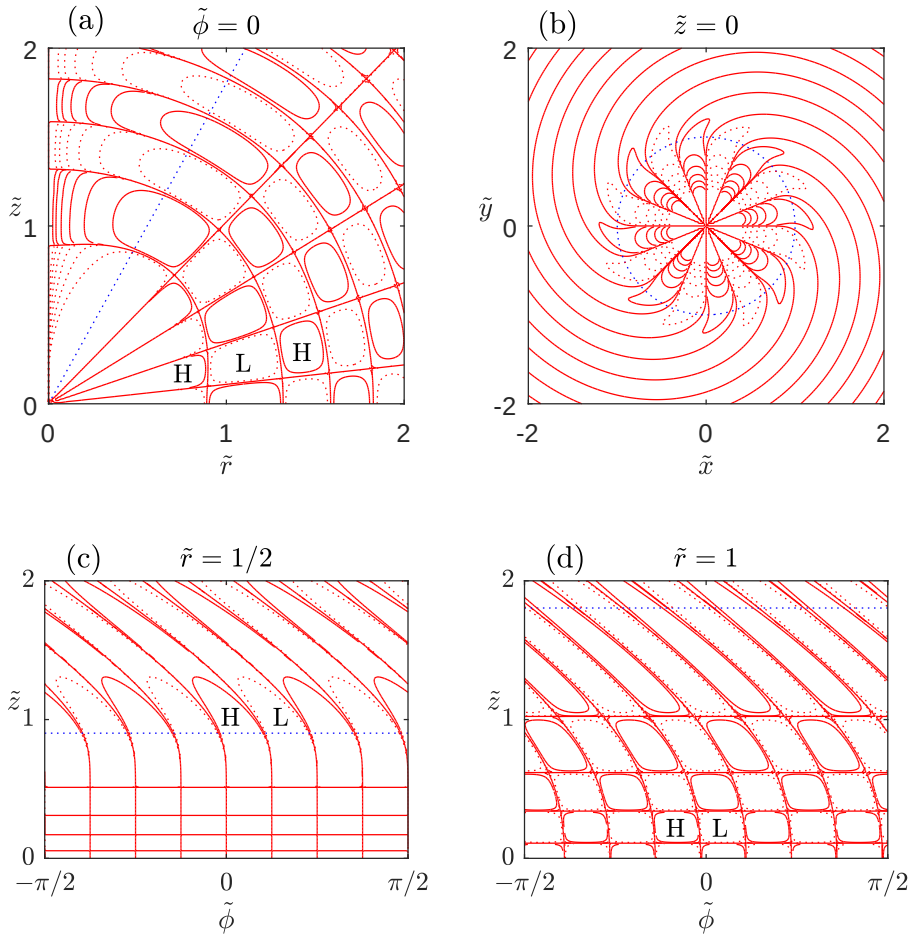

Figure 8. Three-dimensional multipole pressure field: real part of (6.1) for $(n, m) = (16, 8)$, plotted in length units of the sonic radius $r_0 = mc_0/\omega = m/k_0$. Sections are (a) $\tilde{\phi} = 0$; (b) $\tilde{z} = 0$; (c) $\tilde{r} = 1/2$, i.e. half the sonic radius; and (d) $\tilde{r} = 1$, i.e. the sonic radius. (Solid, dotted) curves indicate (positive, negative) pressures; the symbols H and L represent 'high' and 'low'. Contour values are omitted, as the three-dimensional pressure pattern is already clear. The dotted straight lines in (a, c, d) mark the intersections of the plotting surfaces with the cone $\tilde{\theta} = \tilde{\theta}_0 = \sin^{-1}(m/N)$, where $N = n + 1/2 = 16.5$. The dotted circle in (b) is the intersection of the equatorial plane $\tilde{z} = 0$ with the sonic cylinder ($\tilde{r} = 1$ in the length units used). In (a), the implied dependence on $\tilde{\theta}$ at fixed $\tilde{R}$ may be compared with the dependence on x in plot (k) of figure 9; but note the stretching of the x scale required near the polar region $x = 1$, by virtue of the relation $x = \cos\tilde{\theta}$ (for which $\mathrm{d}x/\mathrm{d}\tilde{\theta} = 0$ at $\tilde{\theta} = 0$).

in the spherical coordinates we are using. The amplitude factor a_{nm} is defined by

$$a_{nm} = (-1)^m \frac{(n+m)!}{n!} \frac{N^{N-\frac{1}{2}}}{\{(N-m)^{N-m}(N+m)^{N+m}\}^{\frac{1}{2}}}. \tag{6.5}$$

By means of Stirling's approximation, this factor may be rewritten to high accuracy in terms of gamma functions as

$$a_{nm} \simeq (-1)^m \frac{(n+m)!}{n!} \frac{1}{(N^2-m^2)^{\frac{1}{4}}} \frac{\Gamma(N)}{\{\Gamma(N-m)\Gamma(N+m)\}^{\frac{1}{2}}} g_{nm} \tag{6.6}$$

where g_{nm} is a correction factor defined by

$$g_{nm} = \frac{\left\{\left(1+\frac{1}{12(N-m)}\right)\left(1+\frac{1}{12(N+m)}\right)\right\}^{\frac{1}{2}}}{1+\frac{1}{12N}}. \tag{6.7}$$

Approximation (6.3) is a special case of the asymptotic formula for the Jacobi polynomials derived in [18]; the amplitude factor and its gamma function form (without the correction term) are given there explicitly for an arbitrary Jacobi polynomial, and in obtaining ψ_{e} from [18] we have used common trigonometric identities. These require some care in keeping track of the correct choice of the phase.

Corresponding to the exponential form (4.3) we have

$$P_n^m(x) \simeq \frac{1}{(2\pi)^{\frac{1}{2}}} a_{nm} \frac{\mathrm{e}^{\chi_{\mathrm{p}}(x)}}{(x^2-\hat{x}_0^2)^{\frac{1}{4}}} \qquad (m \geq 0; \quad \hat{x}_0 < x \leq 1) \tag{6.8}$$

where

$$\chi_{\mathrm{p}}(x) = \frac{1}{2} N \ln\left(\frac{x+(x^2-\hat{x}_0^2)^{\frac{1}{2}}}{x-(x^2-\hat{x}_0^2)^{\frac{1}{2}}}\right) - \frac{1}{2} m \ln\left(\frac{x+[(x^2-\hat{x}_0^2)/(1-\hat{x}_0^2)]^{\frac{1}{2}}}{x-[(x^2-\hat{x}_0^2)/(1-\hat{x}_0^2)]^{\frac{1}{2}}}\right) \tag{6.9}$$

and a_{nm} is given as before by (6.5)–(6.6). The subscript p on χ_{p} stands for 'polar', reflecting the fact that (6.8) is suitable for a region surrounding $\tilde{\theta}=0$. As earlier, a symbol involving χ is for a logarithmic measure of amplitude dependence, whereas a symbol involving ψ is for a phase. In all, we have defined χ_{p} and ψ_{e} (polar and equatorial) for associated Legendre polynomials, but χ_{n} and ψ_{f} (near-field and far-field) for Bessel functions.

The simplest way to obtain (6.8) is by analytic continuation from (6.3), in the same way that the Debye approximation (4.3) in χ_{n} may be obtained by analytic continuation from the corresponding form (4.8) in ψ_{f}; and indeed, the formal similarity between the two pairs of formulae is evident. Alternatively, (6.8) may be obtained by the method of [18], allowing for the different position of the saddle points when $x>\hat{x}_0$ compared with $x<\hat{x}_0$, after a coalescence at the turning point $x=\hat{x}_0$.

Instead of (4.10) and (4.5), we have

$$\frac{\mathrm{d}\psi_{\mathrm{e}}}{\mathrm{d}x} = \frac{N(\hat{x}_0^2-x^2)^{\frac{1}{2}}}{1-x^2}, \qquad \frac{\mathrm{d}\chi_{\mathrm{p}}}{\mathrm{d}x} = -\frac{N(x^2-\hat{x}_0^2)^{\frac{1}{2}}}{1-x^2}. \tag{6.10}$$

The extra factor N arises because the associated Legendre polynomials are defined in a bounded range of x, but the Bessel functions in an unbounded range. This also explains the extra factors N and m in (6.4) and (6.9) as compared with (4.4) and (4.9).

(c) Numerical accuracy of the asymptotic formulae

In plots we apply a normalising factor $\left\{(N/(2\pi))(n-m)!/(n+m)!\right\}^{\frac{1}{2}}$ to $P_n^m(x)$ and write the resulting scaled form as $\tilde{P}_n^m(x)$. The same factor is applied to to the asymptotic approximations superposed on plots. Figure 9 gives these plots for $n=1,2,8$, and 16 and a range of m, including the extreme values $m=0$ and $m=n$ in each case. The accuracy of the approximations as a function of x has the same form as for the Bessel function plots in figure 7. That is, the accuracy is high except within a quarter wave of the turning point, now at $x=\hat{x}_0=m/N=m/(n+\frac{1}{2})$ marked with a vertical dotted red line. For all parameter values, either (6.5) or (6.6) may be used for the amplitude factor a_{nm}, as the resulting approximations (dashed lines in the plots) are indistinguishable. If the correction factor g_{nm} in (6.7) is omitted from approximation (6.6) for a_{nm}, there is some loss of accuracy, but this is small, and for many purposes g_{nm} could be omitted for all n and m.

The multipole (6.1) contains $P_n^m(\cos\tilde{\theta})$, where $\tilde{\theta}$ is the polar angle; thus the turning-point $x=\hat{x}_0=(N^2-m^2)^{\frac{1}{2}}/N$ as given in (6.4) corresponds to $\tilde{\theta}=\tilde{\theta}_0=\sin^{-1}(m/N)$. For simplicity, we restrict ourselves to the northern hemisphere $0\leq\tilde{\theta}\leq\pi/2$, and then a natural terminology is that

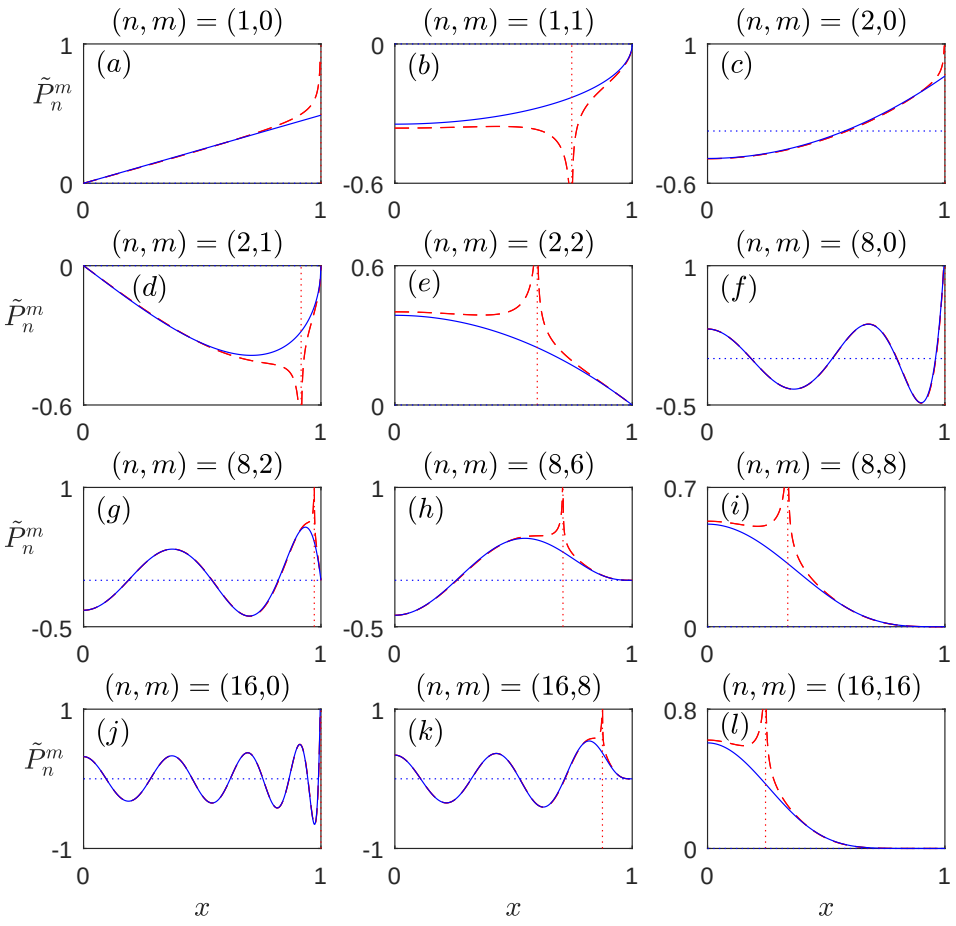

Figure 9. Associated Legendre polynomials in the scaled form $\tilde{P}_n^m(x)$ defined in §6(c), for a range of values of n and m. The solid lines are the exact curves, and the dashed lines are the approximations in §6(b) with a_{nm} in the form (6.5) or (6.6) (this makes no visible difference). The vertical dotted line is at the turning point $x = \hat{x}_0 = (N^2 - m^2)^{\frac{1}{2}}/N$ where $N = n + 1/2$. The accuracy of the approximations is similar to that in figure 7 for Bessel functions. With the change of variable $x = \cos\tilde{\theta}$, plot (*k*) gives the $\tilde{\theta}$ dependence at fixed $\tilde{R}$ as displayed in plot (*a*) of figure 8; the parameter values $(n, m) = (16, 8)$ are the same. In the variable $\tilde{\theta}$, plot (*k*) is considerably stretched near $x = 1$, as we noted.

the range $0 \le \tilde{\theta} < \tilde{\theta}_0$ is the polar region, and $\tilde{\theta}_0 < \tilde{\theta} \le \pi/2$ is the equatorial region, corresponding $\hat{x}_0 < x \le 1$ and $0 \le x < \hat{x}_0$ respectively. This is consistent with our use of $\chi_{\rm p}$ and $\psi_{\rm e}$ in (6.8) and (6.3), which represent exponential decay to the right in the plots (towards the pole) and oscillation on the left (throughout the equatorial region), in agreement with the known behaviour of spherical harmonics.

(d) Regions of locally plane waves for a three-dimensional multipole

Our task now is to determine in which regions of space a three-dimensional multipole field is well approximated by a field of locally subsonic plane waves. By the criteria in §3, this requires that the approximating waves satisfy the dispersion relation (1.2), and also that on a conventional plot the exact and approximate waveforms are indistinguishable or nearly so.

How can we find such a field of waves? The method is that of §4. Thus in (6.1) we approximate $P_n^m(\cos\tilde{\theta})$ by the formulae of §6(b) evaluated at $x = \cos\tilde{\theta}$, and $h_n^{(1)}(\omega\tilde{R}/c_0)$ by the formulae of

§4(b) evaluated at $x=\omega\tilde{R}/c_0$. The latter involve $H^{(1)}_{n+1/2}$, by (6.2). Because of the transition at $\tilde{\theta}=\tilde{\theta}_0$ where $\sin\tilde{\theta}_0=m/(n+1/2)$, and, independently, at $\omega\tilde{R}/c_0=n+1/2$, we must consider four cases in total, which define four types of region in three-dimensional space. Equatorial and polar regions have already been defined for the Legendre polynomials, and similarly near field and far field for Bessel functions; hence we may use the terms (equatorial, near), (polar, near), (polar, far), and (equatorial, far), to refer to the four types of three-dimensional region. We shall shortly deal with these in turn. The pairs of terms which arise in the four cases are

$$(\psi_{\rm e},\chi_{\rm n}),\quad (\chi_{\rm p},\chi_{\rm n}),\quad (\chi_{\rm p},\psi_{\rm f}),\quad (\psi_{\rm e},\psi_{\rm f}), \tag{6.11}$$

in which the first term in each pair is evaluated at $\cos\tilde{\theta}$, and the second at $\omega\tilde{R}/c_0$, and the definitions of the functions $\psi_{\rm e},\chi_{\rm p},\chi_{\rm n},\psi_{\rm f}$ are as given in (6.4), (6.9), (4.4), and (4.9). These give the partial derivatives

$$\frac{1}{\tilde{R}}\frac{\partial\psi_{\rm e}}{\partial\tilde{\theta}}=-\frac{N(\cos^2\tilde{\theta}_0-\cos^2\tilde{\theta})^{\frac{1}{2}}}{\tilde{R}\sin\tilde{\theta}},\qquad \frac{1}{\tilde{R}}\frac{\partial\chi_{\rm p}}{\partial\tilde{\theta}}=\frac{N(\cos^2\tilde{\theta}-\cos^2\tilde{\theta}_0)^{\frac{1}{2}}}{\tilde{R}\sin\tilde{\theta}} \tag{6.12}$$

and

$$\frac{\partial\chi_{\rm n}}{\partial\tilde{R}}=\frac{\{N^2-(\omega\tilde{R}/c_0)^2\}^{\frac{1}{2}}}{\tilde{R}},\qquad \frac{\partial\psi_{\rm f}}{\partial\tilde{R}}=\frac{\{(\omega\tilde{R}/c_0)^2-N^2\}^{\frac{1}{2}}}{\tilde{R}}, \tag{6.13}$$

from (6.10) with $\hat{x}_0=\cos\tilde{\theta}_0$ and (4.10) with $x_0=n+1/2=N$. Recall our convention that ψ-quantities represent angles, and χ-quantities represent terms in logarithms of amplitudes—even though $\psi_{\rm f}$ here depends on $\tilde{R}$ rather than $\tilde{\theta}$, and χ_p depends on $\tilde{\theta}$ rather than $\tilde{R}$. The quantities in (6.11)–(6.13) are real, because the domains of the functions are such that the square roots are of positive quantities. Recall also that for simplicity we provide formulae for the northern hemisphere $\tilde{\theta}\le\pi/2$; these extend to the southern hemisphere by the symmetry relation $P^m_n(-x)=(-1)^{n-m}P^m_n(x)$, in which the transformation $x\mapsto -x$ corresponds to $\tilde{\theta}\mapsto\pi-\tilde{\theta}$. In making general remarks about the full three-dimensional geometry of the multipole, we assume that formulae have been extended in this way.

(i) The (equatorial, near) region

With the aid of (6.3) and (4.3), we find that in the (equatorial, near) region, the asymptotic approximation to the multipole (6.1) is the sum of two terms of the form

$$\tilde{p}(\tilde{R},\tilde{\theta},\tilde{\phi})\simeq P_0^{\pm}\,{\rm e}^{-{\rm i}\omega t}\,{\rm e}^{\Phi_{\rm L}+{\rm i}\Phi_{\rm K}^{\pm}} \tag{6.14}$$

where $P_0^{\pm}$ are slowly varying and

$$\Phi_{\rm L}=-\chi_{\rm n}(\omega\tilde{R}/c_0),\qquad \Phi_{\rm K}^{\pm}=\pm\psi_{\rm e}(\cos\tilde{\theta})+m\phi. \tag{6.15}$$

The separate terms $\Phi_{\rm K}^{\pm}$ come from writing the standing wave $\cos(\psi_{\rm e}+\pi/4)$ in (6.3) as half of the sum of the two travelling waves ${\rm e}^{\pm{\rm i}(\psi_{\rm e}+\pi/4)}$ in the normal way, and $P_0^{\pm}$ are obtained as products of terms which do not contain $\psi_{\rm e}$ and $\chi_{\rm n}$.

The partial derivatives in (6.12) and (6.13) determine the gradients

$$\nabla\Phi_{\rm L}=\Big(-\frac{\partial\chi_{\rm n}}{\partial\tilde{R}},\,0,\,0\Big),\qquad \nabla\Phi_{\rm K}^{\pm}=\Big(0,\,\pm\frac{1}{\tilde{R}}\frac{\partial\psi_{\rm e}}{\partial\tilde{\theta}},\,\frac{m}{\tilde{R}\sin\tilde{\theta}}\Big), \tag{6.16}$$

and a short calculation gives

$$|\nabla\Phi_{\rm K}^{\pm}|^2-|\nabla\Phi_{\rm L}|^2=\left(\frac{\omega}{c_0}\right)^2=k_0^2,\qquad \nabla\Phi_{\rm K}^{\pm}\cdot\nabla\Phi_{\rm L}=0. \tag{6.17}$$

Hence the local behaviour of (6.14) in the (equatorial, near) region is that of the sum of two subsonic waves of the form (1.1) with

$$l=|\nabla\Phi_{\rm L}|,\qquad k=|\nabla\Phi_{\rm K}^{+}|=|\nabla\Phi_{\rm K}^{-}|, \tag{6.18}$$

and local axes (x_1, x_2) in the directions of $(\nabla\Phi_{\rm K}^{\pm},\ -\nabla\Phi_{\rm L})$. The vectors $\nabla\Phi_{\rm K}^{\pm}$ have no component in the $\tilde{R}$ direction, so that the subsonic waves propagate at right angles to the radius vector. The local phase Mach number is given by any of the relations (2.6) between k, l, and M, and then (6.18) with (6.16) gives

$$M = \frac{\omega\tilde{R}/c_0}{N}. \tag{6.19}$$

This always gives $M < 1$, because the definition of the near field is $\omega\tilde{R}/c_0 < N$.

(ii) The (polar, near) region

In the (polar, near) region, we obtain similarly the approximation

$$\tilde{p}(\tilde{R}, \tilde{\theta}, \tilde{\phi}) \simeq P_0\, \mathrm{e}^{-\mathrm{i}\omega t}\, \mathrm{e}^{\Phi_{\rm L} + \mathrm{i}\Phi_{\rm K}} \tag{6.20}$$

where P_0 is slowly varying and now

$$\Phi_{\rm L} = \chi_{\rm p}(\cos\tilde{\theta}) - \chi_{\rm n}(\omega\tilde{R}/c_0), \quad \Phi_{\rm K} = m\phi. \tag{6.21}$$

These give

$$\nabla\Phi_{\rm L} = \Big(-\frac{\partial\chi_{\rm n}}{\partial\tilde{R}},\ \frac{1}{\tilde{R}}\frac{\partial\chi_{\rm p}}{\partial\tilde{\theta}},\ 0\Big), \quad \nabla\Phi_{\rm K} = \Big(0,\ 0,\ \frac{m}{\tilde{R}\sin\tilde{\theta}}\Big), \tag{6.22}$$

and a short check shows that these satisfy the locally subsonic plane wave conditions analogous to (6.17)–(6.18), but with

$$M = \frac{(\omega\tilde{R}/c_0)\sin\tilde{\theta}}{m}. \tag{6.23}$$

Since $\omega\tilde{R}/c_0 < N$ and $\sin\tilde{\theta} < m/N$ in the region we are considering, this gives $M < 1$ throughout, as expected. As in the previous case, the subsonic wave propagates at right angles to the radius vector, because the $\tilde{R}$ component of $\nabla\Phi_{\rm K}$ in (6.22) is zero.

(iii) The (polar, far) region

In the (polar, far) region, the analysis is similar, but with

$$\Phi_{\rm L} = \chi_{\rm p}(\cos\tilde{\theta}), \quad \Phi_{\rm K} = \psi_{\rm f}(\omega\tilde{R}/c_0) + m\phi \tag{6.24}$$

and

$$\nabla\Phi_{\rm L} = \Big(0,\ \frac{1}{\tilde{R}}\frac{\partial\chi_{\rm p}}{\partial\tilde{\theta}},\ 0\Big), \quad \nabla\Phi_{\rm K} = \Big(\frac{\partial\psi_{\rm f}}{\partial\tilde{R}},\ 0,\ \frac{m}{\tilde{R}\sin\tilde{\theta}}\Big). \tag{6.25}$$

These satisfy the subsonic plane wave conditions (3.2). The field in this region is striking in being essentially of near-field type, in that the waves within it are entirely subsonic, yet geometrically the region is *exterior* to the sphere $\omega\tilde{R}/c_0 = N$, and extends to infinity. Thus locally subsonic waves are capable of describing non-radiating angular sectors of three-dimensional sound fields. The local phase Mach number M is now a more complicated function of position, but it satisfies the relation

$$\frac{1}{M^2} = 1 + \frac{m^2 - N^2\sin^2\tilde{\theta}}{(\omega\tilde{R}/c_0)^2\sin^2\tilde{\theta}}, \tag{6.26}$$

from which it follows that $M < 1$.

(iv) The (equatorial, far) region

Finally, in the (equatorial, far) region, we have

$$\Phi_{\mathrm{L}} = 0, \quad \Phi_{\mathrm{K}}^{\pm} = \pm\psi_{\mathrm{e}}(\cos\tilde{\theta}) + \psi_{\mathrm{f}}(\omega\tilde{R}/c_0) + m\phi, \tag{6.27}$$

from which

$$\nabla\Phi_{\mathrm{L}} = (0,\ 0,\ 0), \qquad \nabla\Phi_{\mathrm{K}}^{\pm} = \Big(\frac{\partial\psi_{\mathrm{f}}}{\partial\tilde{R}},\ \pm\frac{1}{\tilde{R}}\frac{\partial\psi_{\mathrm{e}}}{\partial\tilde{\theta}},\ \frac{m}{\tilde{R}\sin\tilde{\theta}}\Big). \tag{6.28}$$

We now find that

$$\big|\nabla\Phi_{\mathrm{K}}^{\pm}\big|^2 = \left(\frac{\omega}{c_0}\right)^2 = k_0^2, \tag{6.29}$$

so that in the terminology of §1 we have $(k, l) = (k_0, 0)$ and hence $M = 1$, which means that (6.28) represents two fields of ordinary sonic waves. For completeness, we discuss this case, even though the focus of the paper is subsonic waves. In particular, since (6.29) is the eikonal equation for the wave equation, and the speed of sound c_0 is assumed to be constant, it follows that the rays are straight lines; this fact is somewhat obscured in (6.28) because of the spherical coordinates used.

In (6.28) the first component of $\nabla\Phi_{\mathrm{K}}^{\pm}$ vanishes when $\omega\tilde{R}/c_0 = N$, by (6.13), and so the rays are tangent to the sphere $\tilde{R} = Nc_0/\omega$. This is a most significant fact: although one might think of the far field straight-line rays of the multipole field (6.1) as having come from the origin, this is not really so. In fact, they come from the sphere $\tilde{R} = Nc_0/\omega = (n + \frac{1}{2})c_0/\omega$ as tangents, as if the sound were generated here rather than at the origin. We shall not pursue this line of reasoning, but merely note that just outside the sphere these straight-line rays do not point even approximately along the radius vector away from the origin, but instead point in an almost perpendicular direction to this. It is necessary for $\tilde{R}$ to be as large as order N^2c_0/ω for the angle between the rays and the radius vector to be as small as order $1/N$. Thus the region of space in which the straight line rays are not closely radial can be very large—a fact of importance for the scattering of a three-dimensional multipole field by a body in its vicinity, because the directivity pattern of the scattered field depends strongly on the incident ray direction.

(e) Accuracy of the locally plane wave representation

The domain of accuracy of the plane wave representations just given can be determined by inspecting the plots in figures 7 and 9 for Bessel functions and associated Legendre polynomials. Both functions need to be well approximated; hence a local plane wave approximation to a three-dimensional multipole is accurate everywhere except in a spherical annulus centred on the sphere defined by $\omega\tilde{R}/c_0 = N = n + \frac{1}{2}$ and in conical annuli centred on the cones $\theta = \tilde{\theta}_0$ and $\theta = \pi - \tilde{\theta}_0$, where $\sin\tilde{\theta}_0 = m/N = m/(n + \frac{1}{2})$. Therefore the important question is the widths of these annuli as a function of the multipole parameters (m, n). The plots show that for nearly all values of m and n the annuli are narrow in relation to the total region over which one might hope to use plane wave approximations, the main exception being that for m close to or equal to n the conical annuli are rather wide. Thus apart from this case, a three-dimensional multipole can be well represented by a locally plane wave in a larger region of space than might have been expected.

The explanation of the above results is that the sphere and the two cones are envelopes of rays, i.e. are caustics, and it is known that ray representations fail to describe solutions of the wave equation in a caustic zone extending one-quarter wave either side of the caustic [19]. Since the local plane wave representation determines a field of rays, with ray directions $\nabla\Phi_{\mathrm{K}}$ or $\nabla\Phi_{\mathrm{K}}^{\pm}$, and the annuli defined in the previous paragraph are of just the size of the caustic zone, it follows that no locally plane wave description could have visibly better numerical performance than that found here: that is, our approach based on $(\psi_{\mathrm{e}}, \chi_{\mathrm{p}}, \chi_{\mathrm{n}}, \psi_{\mathrm{f}})$ finds the local plane waves in the multipole field (6.1) everywhere they exist, and then gives them accurately through the approximations in §4(a, b) and §6(b) for the Bessel functions and associated Legendre polynomials.

7. Conclusions and further work

In the present work we have confined ourselves to two core mathematical aspects of our approach. These are, first, an analytical description of the distant scattered field produced by a small sphere when irradiated by a subsonic plane wave; and second, a determination of regions of space in which a near field is well approximated at each point by a such a subsonic wave. We have carried out the latter for three families of incident fields, of cylindrical, helical, and three-dimensional multipole type, including not only a full mathematical analysis of these regions for each family, but also numerical comparisons of exact and asymptotic formulae to reveal the size of the regions. The conclusion is that the regions are rather large in general, and therefore that the theory we present is potentially of broad scope.

Many developments of the work suggest themselves, especially oriented to applications, and two in particular stand out. The first is a numerical study of the degree of accuracy of the method as a function of the main parameters in the problem, namely the radius of the scatterer, its position in the near field, and the type of boundary condition imposed on its surface. We have begun a study of this matter by the T-matrix methods developed in [10,11], and the results will be reported elsewhere. The second is the relation of the work to many existing approaches to multiple-scattering problems. The key point here is that in multipole methods arising from separation of variables [7, p. 138], each scatterer is in the near field of all the other scatterers for which the condition 'argument is less than order' is satisfied for at least one significant multipole term. Hence physically, a large part of the mutual scattering effect is indeed caused by near-field scattering of locally subsonic waves, and the question arises of whether this fact could be incorporated into a full asymptotic theory, or a fully implemented numerical approach.

In the multipole context, note that these locally subsonic near-field waves propagate at right angles to the radius vector from the source to the scatterer—perhaps in contradiction to intuition based on scattering in the remote far field of a source, where the incident wave propagates *along* the radius vector. Nevertheless, this counter-intuitive aspect of near-field ray geometry is strikingly evident in the three examples worked out, and is especially clear in figure 8. To understanding near-field scattering, the direction of these incident waves is the most important thing to get right.

We see the above ideas as most useful for future work, possibly leading to an enhancement of existing numerical methods. More generally, our approach applies to many types of wave field throughout physics and the applied sciences, including not only acoustic, electromagnetic, and elastic waves, but also many others besides.

Authors' Contributions. CJC instigated the subsonic wave approach, performed the mathematical analysis, and wrote the first draft of the paper. SH created the algorithms for computer coding, identified key aspects of the numerical work, and edited/reviewed the final draft.

Competing Interests. We have no competing interests.

Funding. The authors would like to thank the Isaac Newton Institute for Mathematical Sciences, Cambridge, for support and hospitality during the programme Mathematical Theory and Applications of Multiple Wave Scattering where work on this paper was undertaken. The work was supported by EPSRC grant no. EP/R014604/1&34. SH gratefully acknowledges funding by the Australian Research Council (ARC), grant DP220102243, and also the Simons Foundation for support to attend the programme.

Data Accessibility. The paper does not report primary data.

Ethics. The research did not involve human or animal subjects.

Acknowledgements. CJC's work was supported at Keele University through Research Excellence Framework funds. We thank a referee for for providing the stimulus to carry out the multipole analysis of §6. This has added greatly to the usefulness of the work.

References

1. Brekhovskikh LM. 1980 *Waves in layered media*. 2nd edn. New York: Academic.
2. Choudhary S, Felsen LB. 1973 Asymptotic theory for inhomogeneous waves. *IEEE Trans. Antennas Prop.* **AP-21**, 827–842. (doi:10.1109/TAP.1973.1140598)
3. Wang WD, Deschamps GA. 1974 Application of complex ray tracing to scattering problems. *Proc. IEEE* **62**, 1541–1551. (doi:10.1109/PROC.1974.9661)
4. Felsen LB. 1976 Evanescent waves. *J. Opt. Soc. Am.* **66**, 751–760. (doi:10.1364/JOSA.66.000751)
5. Bowman JJ, Senior TBA, Uslenghi PLE (eds). 1987 *Electromagnetic and acoustic scattering by simple shapes*. New York: Hemisphere.
6. Dassios G, Kleinman R. 2000 *Low frequency scattering*. Oxford: OUP.
7. Martin PA. 2006 *Multiple scattering: interaction of time-harmonic waves with N scatterers*. Cambridge: CUP.
8. Lighthill J. 1978 *Waves in fluids*. Cambridge: CUP.
9. Howe MS. 2015 *Acoustics and aerodynamic sound*. Cambridge: CUP. (doi:10.1017/CBO9781107360273)
10. Ganesh M, Hawkins SC. 2017 Algorithm 975: TMATROM—A T-matrix reduced order model software. *ACM Trans. Math. Software* **44**, 9, 1–18. (doi:10.1145/3054945)
11. Barkhan J, Ganesh M, Hawkins SC. 2022 Approximation of radiating waves in the near-field: error estimates and application to a class of inverse problems. *J. Comp. Appl. Math.* **404**, 113769, 1–19. (doi:10.1016/j.cam.2021.113769)
12. Chapman CJ. 2001 Energy paths in edge waves. *J. Fluid Mech.* **426**, 135–154. (doi:10.1017/S0022112000002184)
13. Chapman CJ. 1994 Sound radiation from a cylindrical duct. Part I. Ray structure of the duct modes and of the external field. *J. Fluid Mech.* **281**, 293–311. (doi:10.1017/S0022112094003113)
14. Olver FWJ, Lozier DW, Boisvert RF, Clark CW. 2009 *NIST handbook of mathematical functions*. Cambridge: CUP; also *NIST Digital Library of Mathematical Functions*. https://dlmf.nist.gov/
15. Olver FWJ. 1974 *Asymptotics and special functions*. London: Academic.
16. Prentice PR. 1992 The acoustic ring source and its application to propeller acoustics. *Proc. R. Soc. Lond. A* **437**, 629–644. (doi:10.1098/rspa.1992.0083)
17. Chapman CJ. 1993 The structure of rotating sound fields. *Proc. R. Soc. Lond. A* **440**, 257–271. (doi:10.1098/rspa.1993.0015)
18. Gil A, Segura J, Temme NM. 2021 Asymptotic expansions of Jacobi polynomials and of the nodes and weights of Gauss-Jacobi quadrature for large degree and parameters in terms of elementary functions. *J. Math. Anal. Appl.* **494**, 124642, 1–14. (doi:10.1016/j.jmaa.2020.124642)
19. Kravtsov Yu. A, Orlov Yu. I. 1993 *Caustics, catastrophes and wave fields*. New York: Springer.